POLITECNICO DI TORINO
Repository ISTITUZIONALE

Satellite Precipitation Measurements: What Have We Learnt About Cloud-Precipitation Processes From Space?

Original
Satellite Precipitation Measurements: What Have We Learnt About Cloud-Precipitation Processes From Space? / Kikuchi, M., Braun, S.A., Suzuki, K., Liu, G., Battaglia, A. - In: Clouds and Their Climatic Impacts[s.l] : AGU, 2023. - ISBN 9781119700319. - pp. 303-324 [10.1002/9781119700357.ch15]

Availability:
This version is available at: 11583/2990119 since: 2024-07-01T15:41:59Z

Publisher:
AGU

Published
DOI:10.1002/9781119700357.ch15

Terms of use:

This article is made available under terms and conditions as specified in the corresponding bibliographic description in the repository

Publisher copyright
AGU

Da definire

(Article begins on next page)

26 November 2026

15

Satellite Precipitation Measurements: What Have We Learnt About Cloud-Precipitation Processes From Space?

Maki Kikuchi[1], Scott A. Braun[2], Kentaroh Suzuki[3], Guosheng Liu[4], and Alessandro Battaglia[5,6]

ABSTRACT

Precipitation is one of the fundamental elements that define global and regional climatology. Precipitation systems consist of a broad spectrum of three-dimensional structures in which microphysical processes interact with macroscale processes in the cloud system and the ambient environment that prescribe the evolution of the system. Since 1970s, satellite observations of precipitation have been a fundamental tool in quantifying this complex interaction. They have first quantified the frequency and intensity of global precipitation, including remote areas over open oceans and polar regions, thus providing today's precipitation climatology. More recently, satellite observations of cloud and precipitation have been exploited for understanding the physical mechanisms governing precipitation systems. A subset of these studies also provided observation-based metrics to probe physical processes operating in cloud-precipitation systems and to apply them as diagnostic measures for evaluating the representation of the processes in numerical models for better projections of future climate. In this chapter, we review the theoretical basis of precipitation remote sensing from space and describe how it is practically applied in satellite missions. In the first part of the chapter, a historical overview of the satellite missions is described, summarizing the instruments and retrieval algorithms developed in the missions. In the second part, we introduce a set of studies discussing the fundamental mechanisms behind precipitation formation, highlighting what we have learnt to date on cloud-precipitation processes from satellite observations.

15.1. INTRODUCTION

Precipitation is condensed water (liquid and ice particles or their mixtures) that forms in clouds when cloud particles grow large enough to fall. Precipitating particles are distributed vertically in the atmosphere and fall typically as rain, snow, graupel, or hail. As cloud growth and precipitation formation progress, they supply water to the surface, constituting a major component in the hydrological cycle. Precipitation also plays a fundamental role in the Earth's energy budget. When solar energy is consumed to evaporate the surface water, energy is transported through the atmosphere as latent heat associated with water vapor. The latent heat is then released to warm the atmosphere via condensation and deposition processes, thus moving the energy from the surface to atmosphere.

In precipitation formation, there are several paths for cloud particles to grow into precipitation. In warm clouds where clouds are entirely composed of liquid droplets, precipitation is formed through a microphysical process

[1]*Earth Observation Research Center, Japan Aerospace Exploration Agency, Ibaraki, Japan*
[2]*NASA Goddard Space Flight Center, Greenbelt, MD, USA*
[3]*Atmosphere and Ocean Research Institute, The University of Tokyo, Chiba, Japan*
[4]*Department of Earth, Ocean and Atmospheric Science, Florida State University, Tallahassee, FL, USA*
[5]*Department of Environment, Land and Infrastructure Engineering, Polytechnic University of Turin, Turin, Italy*
[6]*Department of Physics and Astronomy, University of Leicester, Leicester, UK*

Clouds and Their Climatic Impacts: Radiation, Circulation, and Precipitation, Geophysical Monograph 281, First Edition.
Edited by Sylvia C. Sullivan and Corinna Hoose.
© 2024 American Geophysical Union. Published 2024 by John Wiley & Sons, Inc.
DOI: 10.1002/9781119700357.ch15

called *warm-rain processes*. During this process, the cloud droplets are formed by condensation of water vapor and become larger by swelling water vapor further until they reach a certain size (typically around 15–20 μm). Beyond this size, the process is replaced by *collision and coalescence*, where larger droplets grow by collecting surrounding smaller droplets. In cold clouds under subfreezing temperatures, *cold-rain processes* become the dominant precipitation mechanism. Whenever ice and liquid coexist, ice crystals grow rapidly at the expense of liquid droplets by the *Wegener-Bergeron-Findeisen (WBF) process*, where the liquid droplets evaporate and serve as a continuous source of water vapor to ice crystals due to the lower saturation vapor pressure of ice compared to that of liquid (Bergeron, 1935; Findeisen, 1938; Wegener, 1911). Other mechanisms for ice particle growth involve liquid-ice and ice-ice interactions, including *riming* where supercooled droplets freeze directly onto the crystal surface and *aggregation* where crystal arms of multiple particles stick together to form one larger particle. Latent heat is released during most of these processes (e.g., vapor deposition and freezing of liquid to ice) and heats the surrounding atmosphere which invigorates convection and precipitation formation. Ultimately, these ice crystals become large enough to fall as snow, or otherwise melt to form rain drops.

What makes the precipitating cloud systems complex is the fact that these microphysical processes, typically occurring at the scale of micrometers to millimeters, underpin individual convective storms (of few kilometers in size) that interact with large-scale dynamics to generate larger systems such as mesoscale convective systems (MCS) (see also Chapter 9: An Overview of Mesoscale Convective Systems). Such a wide spectrum of scales with high temporal and spatial variabilities makes it challenging to quantify precipitation over the globe. For over a century, rain gauges have been providing detailed observations essential to characterizing the surface precipitation. Later, satellite mission concepts were considered with the aim to understand global precipitation and its impact on climate given that the area covered by gauges is rather limited, equivalent to "less than half a football field" (Kidd et al., 2017). It was in the 1970s when Earth observation from satellites started. Thanks to subsequent measurement advances, our understanding of global precipitation has improved drastically, particularly for its frequency and intensity across the globe, enabling better characterization of precipitation climatology. Building upon these advances, a number of studies have been devoted to analyzing multiple satellite measurements to examine not only precipitation itself but also its interactions with cloud, radiation, and the ambient environment, in an attempt to reveal signals of precipitation-related processes behind the snap-shot observations.

Generally speaking, the term "process" refers to a mechanism responsible for a temporal change in physical states. With regard to precipitation, the relevant processes include microphysical and thermodynamical changes of hydrometeors themselves (e.g., particle evolutions, phase changes, and the resultant radiative changes), as well as dynamical changes in the cloud system (e.g., latent heat impact on storm invigoration). These "internal" processes interact with "external" factors including aerosols (e.g., aerosol seeding of cloud droplets or crystals, precipitation removal of aerosols, aerosol impacts on precipitation, and radiative forcing associated with them) and further interact on broader factors related to land-surface and cryospheric processes, the water cycle and the radiation budget of the Earth. The search for a deeper understanding of these physical processes governing precipitation has leveraged studies linking individual measurement data to diagnostics of the related processes underpinning the observed precipitation beyond scrutinizing precipitation climatology, the evolution of these processes in a warming climate, and better representation of the processes in numerical models (Stephens et al., 2018).

In this chapter, an overview of the progress in satellite precipitation measurement is addressed, with a particular focus on outlining the insights into precipitation-related processes obtained from recent studies. Section 15.2 reviews the fundamental principles of precipitation measurement in satellite remote sensing. The historical overview of satellite precipitation measurement and their retrieval algorithms are described in section 15.3. Selected examples of observation-based analysis of cloud-precipitation processes are then highlighted in section 15.4. Future satellite missions planned for precipitation measurement to further advance cloud-precipitation science are discussed in section 15.5. Note that the chapter highlights recent advances in cloud-precipitation processes rather than on water vapor processes, although some aspects of water vapor in convective processes are touched upon. Finally, the chapter is summarized in section 15.6.

15.2. SATELLITE REMOTE SENSING OF PRECIPITATION – PHYSICAL BASIS

Hydrometeors emit, absorb, and scatter radiative energy and precipitation remote sensing seeks to convert the radiative energy received by a satellite-borne radar or radiometer to water flux at the surface. Therefore, the physical basis of retrieving precipitation involves two fundamental relations, that is, (1) how hydrometeors interact with radiation, which is often determined by their size, shape, and single-scattering properties and (2) how microphysical properties distributed in the vertical column relate to surface water flux, which

10.1002/9781119700357.ch15, Downloaded from https://agupubs.onlinelibrary.wiley.com/doi/10.1002/9781119700357.ch15 by Maki Kikuchi - Cochrane Japan , Wiley Online Library on [21/12/2023]. See the Terms and Conditions (https://onlinelibrary.wiley.com/terms-and-conditions) on Wiley Online Library for rules of use; OA articles are governed by the applicable Creative Commons License

depends on the vertical variability of natural precipitating clouds. For radars, the second relation is less of an issue since radar reflectivity can be determined in individual atmospheric layers. However, in the case of passive remote sensing by radiometers, the vertical distribution of hydrometeors plays a critical role in determining satellite-observed radiative energy. Thus, early SSM/I-era retrieval methods relied on statistical relations between hydrometers aloft and precipitation rate at the surface (Grody, 1991).

For passive remote sensing, satellite received radiances come from either reflected sunlight or thermal emission by targets in the sensor's field of view. Precipitating clouds are opaque in the visible and infrared spectrum and precipitation estimations in these spectral ranges are chiefly related to the cloud top structure, relying on the second relation mentioned above. The general assumption is that the more reflective or the taller the cloud top is, the more intense the precipitation will be at the surface. In the microwave (including millimeter wave) spectrum, however, the satellite received radiation is a result of scattering/emission of the surface emission as it interacts with all hydrometeors and constituent gases throughout the entire atmospheric column, and the absorption and scattering by hydrometeors dictate the upwelling radiative energy. Using the frequency of 166 GHz, which is used in Global Precipitation Measurement mission microwave imager, as an example, the absorption and scattering properties of several types of hydrometeors in this wave spectrum are shown in Figure 15.1. Because radiation at higher frequencies is more sensitive to ice scattering, the 166 GHz is used here to make a clear contrast among the scattering properties by different types of hydrometeors. In this figure, raindrops and hail are assumed to be spheres with density of 1.0 and 0.8 g/cm^3, respectively, while dendrite crystals and aggregates are taken from ice scattering database of Liu (2008) and Nowell et al. (2013). First of all, absorption by ice particles is about 2 orders of magnitude weaker than that by liquid drops, which gives rise to little emission by ice particles in the microwave spectrum. Second, given the same liquid-equivalent radius (or mass), the scattering intensity depends strongly on particle shape, which dramatically complicates the retrieval problem because of the large variety of ice particle shapes in natural clouds.

Due to the relative transparency of the atmosphere in the microwave spectrum, surface emissivity is another impacting factor on upwelling radiation. Emissivity over ocean is polarized with a magnitude lower than unity, and fairly well modeled except at high wind conditions (Kilic et al., 2019), while over land it is high (close to 1) and highly variable. As explained above, passive microwave precipitation remote sensing relies on emission and scattering signatures from hydrometeors. Generally speaking, the emission signature is generated from liquid drops that enhances upwelling radiances over ocean at low frequencies (e.g., <80 GHz) and is less of an influence over most land surfaces because of the near 0.9 surface emissivity. On the other hand, the scattering signature is generated by ice particles and only strong enough at high frequencies, although it can be observed over both land and ocean. Therefore, precipitation retrieval

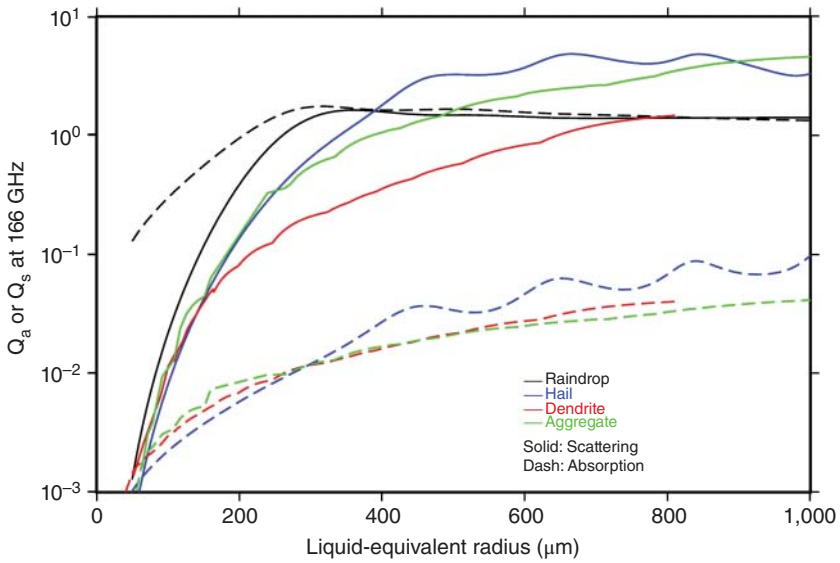

Figure 15.1 Scattering and absorption at 166 GHz for raindrop, hail, dendrite crystal, and ice aggregate. Q_s and Q_a are defined by the scattering and absorption cross-sections divided by cross-section area of a liquid-equivalent drop.

10.1002/9781119700357.ch15, Downloaded from https://agupubs.onlinelibrary.wiley.com/doi/10.1002/9781119700357.ch15 by Maki Kikuchi - Cochrane Japan , Wiley Online Library on [21/12/2023]. See the Terms and Conditions (https://onlinelibrary.wiley.com/terms-and-conditions) on Wiley Online Library for rules of use; OA articles are governed by the applicable Creative Commons License

by passive microwave observations is based on the assumption that a greater amount of liquid or ice water in the atmospheric column leads to heavier precipitation at surface. Although this relation is more direct than the cloud top-precipitation relation assumed for visible and infrared remote sensing, it is still a large source of error, especially for the ice-precipitation relation assumed for scattering signatures.

For active remote sensing by radars, the observed signature is the backscattered energy by hydrometeors in a finite volume (namely, radar reflectivity). The relation between radar reflectivity and precipitation rate depends strongly on the particle size distribution. The satellite dual-frequency radar measurements (explained in section 15.3) are introduced to minimize this uncertainty, in which one frequency operates in the Rayleigh and the other operates in the non-Rayleigh regime. Assuming that the particle size distribution can be expressed by a two-parameter function – for example, mean diameter and total particle number – the precipitation rate can then be uniquely determined by the two radar reflectivity values. As in passive remote sensing, additional complication arises for retrieving solid precipitation (i.e., snowfall), in which ice particles are non-spherical with a large variety of shapes, and often have preferred orientations.

In the next section, we introduce how these theoretical characteristics of precipitation remote sensing are practically applied in the precipitation measurement from space.

15.3. HISTORICAL OVERVIEW OF SATELLITE PRECIPITATION REMOTE SENSING

15.3.1. Passive Remote Sensing

Building upon the principles explained above, satellite precipitation remote sensing has essentially two pillars of observation techniques: active remote sensing by microwave radars and passive remote sensing by microwave radiometers. Passive microwave instrumentation had undergone multiple generational upgrades since the earliest single-frequency imager was used for precipitation remote sensing in the 1970s (Wilheit, 1972); current satellite microwave imagers in operation cover frequencies from 6 to 183 GHz and make measurements at both horizontal and vertical polarizations (Aonashi & Ferraro, 2020), among which the following sensors are worth mentioning. First, the Special Sensor Microwave Imager (SSM/I) was a conically scanning radiometer operating at frequencies near 19, 22, 37, and 85.5 GHz with dual polarizations at all but the 22 GHz channel (Hollinger et al., 1987). With its multispectral coverage and stable calibration, the SSM/I is often considered to mark the start of the modern era for microwave radiometry for precipitation (Kummerow, 2020); most currently operational radiometers can find their roots from SSM/Is. For example, the Tropical Rainfall Measuring Mission (TRMM) Microwave Imager (TMI) operated at channels similar to SSM/I, with added channels at a lower frequency of 10.7 GHz, and the Advanced Microwave Scanning Radiometer (AMSR) series further adds channels near 7 GHz, primarily for ocean surface parameter retrievals. The Special Sensor Microwave Imager/Sounder (SSMIS) continues the legacy of SSM/I, but consolidates channels previously covered by two other sounding sensors on the Defense Meteorological Satellite Program (DMSP) satellites to include channels near 60 GHz oxygen and 183 GHz water vapor absorption frequencies and at a 150 GHz window frequency. Likewise, the Global Precipitation Measurement (GPM) mission microwave imager (GMI) continues the legacy of TMI but includes observations at higher frequencies of 166 and 183 GHz mainly for snowfall estimation. Most modern era microwave radiometer precipitation algorithms have their origins in concepts developed earlier with SSM/I observations.

Satellite microwave radiometer received energy (as expressed by equivalent blackbody brightness temperature, or TB) is an integral of the emission, absorption, and scattering from the surface, atmospheric gases, and hydrometeors. Because of the complexity involved in the combinations of these geophysical variables, any given set of observed brightness temperatures could correspond to a number of precipitation rates. In other words, the retrieval problem is ill-conditioned with multiple solutions from a single input. To obtain a reasonable solution, retrieval algorithms must set some constraints to reduce the range within which the solution is to be searched. In the following, we briefly describe how satellite algorithms retrieve precipitation rates, by taking the GPM's Goddard Profiling (GPROF) algorithm (Kummerow et al., 2015) as an example. The GPROF algorithm retrieves precipitation using the Bayes' theorem with an *a priori* database linking hydrometeor profiles and brightness temperatures. Estimation is computed by a weighted average of precipitation rates for those profiles that are radiometrically consistent with observations, and the weights are determined by the distance between observed and database brightness temperature vectors. The key component of the algorithm is the *a priori* database in which the hydrometeor profiles need to be representative to those occurring in nature. The most current version uses hydrometeor profiles retrieved from the GPM radar-radiometer combined algorithm (Grecu et al., 2016) and their associated brightness temperatures are computed by radiative transfer simulations. To constrain the algorithm solution by the associated environmental conditions, ancillary data of surface class,

10.1002/9781119700357.ch15, Downloaded from https://agupubs.onlinelibrary.wiley.com/doi/10.1002/9781119700357.ch15 by Maki Kikuchi - Cochrane Japan , Wiley Online Library on [21/12/2023]. See the Terms and Conditions (https://onlinelibrary.wiley.com/terms-and-conditions) on Wiley Online Library for rules of use; OA articles are governed by the applicable Creative Commons License

2-m temperature, and precipitable water are introduced to subset the database, so that solutions can only be found in a specified portion within the database.

With the advantage of frequent sampling, visible and infrared measurements, particularly from geostationary satellites, have also played an important role in precipitation retrieval. The imaging spectroradiometers onboard these platforms have gradually evolved in spectral, spatial, and temporal resolution. For example, the Advanced Baseline Imager (ABI) on the GOES-R Series and the Advanced Himawari Imager (AHI) on the Himawari-8 satellites can produce a full disk image every 10–15 minutes with 0.5–2 km spatial resolution; both instruments have 16 channels covering 0.455–13.3 μm wavelength. Due to the physical indirectness to surface precipitation, visible/infrared retrieval algorithms are prone to large errors. To compensate for this shortcoming, techniques have been introduced to estimate precipitation total over a long time and a large area, for example, the GOES Precipitation Index (GPI, Arkin & Meisner, 1987). On the other hand, efforts for instantaneous precipitation retrieval have been made by classifying clouds using horizontal texture, cloud-patch identification, and multi-spectral information (Adler & Negri, 1988; Ba & Gruber, 2001; Bellerby, 2004; Behrangi et al., 2009; Hong et al., 2004). Taking the advantage of frequent sampling by infrared measurements and the physical directness of microwave measurements, some great successes have been reported recently by combining the two, in which microwave retrievals are used to calibrate the infrared algorithm while infrared measurements are used to enhance spatial and temporal coverages of precipitation estimates (Huffman et al., 2007; Hsu & Sorooshian, 2009; Joyce & Xie, 2011; Ushio et al., 2009).

15.3.2. Active Remote Sensing

Radars represent the other pillar of precipitating cloud remote sensing, as demonstrated by the continuous operation record of the three major atmospheric radar missions in the past 22 years: the TRMM, CloudSat, and the GPM mission. Figure 15.2 illustrates the timeline of the launch and operational period of the missions. The launch (November 1997) of the TRMM Ku-band (13.6 GHz) Precipitation Radar (PR), part of a joint mission between the National Aeronautics and Space Administration (NASA) and the Japanese Aerospace Exploration Agency (JAXA), spearheaded a new era of space-borne atmospheric radar missions (Kummerow et al., 2000). The TRMM PR was the first weather radar in space providing unprecedented three-dimensional (3D) structure of storm systems (Houze Jr. et al., 2015; Okamoto, 2003), mapping precipitation over a swath of more than 215 km with a 250 m vertical resolution. The TRMM PR was followed (in April 2006) by the NASA CloudSat W-band (94 GHz) Cloud Profiling Radar (CPR) (Tanelli et al., 2008) as part of the A-Train, a constellation of active and passive instruments in a sun-synchronous orbit with ascending equatorial crossing around 1:30 p.m. local solar time. Thanks to its superior sensitivity and its synergy with other instruments in the A-Train (Stephens et al., 2018), the CloudSat CPR has provided the first ever collection of global vertical profile observations not only of clouds but also of light rain and snow (Lebsock et al., 2020). The global precipitation record begun by TRMM was continued with the launch (February 2014) of the GPM-core observatory (Skofronick-Jackson et al., 2018). The GPM Dual-frequency Precipitation Radar (DPR), the first of its kind to be flown in space with the Ku-band (13.6 GHz) and Ka-band (35.5 GHz) radars (Iguchi, 2020), expands the capability of the TRMM PR in terms of coverage of high latitudes and improved sensitivity, thus enabling detection of lighter precipitation and snow (Kidd et al., 2020).

The diverse capabilities of these different radar systems, spanning frequencies from Ku to W band, are demonstrated in the GPM and CloudSat coincident observations of a precipitation system over the Gulf of Thailand (top panels of Fig. 15.2). The CloudSat CPR depicts a cloud system extending up to 15 km, including three precipitating clusters with a melting layer at about 5 km and an upper cirrus cloud anvil. The CPR signal is attenuated in the rain region below the melting layer and decreases below the noise level in correspondence to the first rain cell at around 80 km along-track distance. As an indication of the attenuation of the signal the path integrated attenuation (PIA) derived from the surface reference technique (Meneghini et al., 2015) is overplotted as a black line on all reflectivity panels in Figure 15.2. The GPM DPR misses most of the ice cloud but can easily penetrate the rain layer, with different levels of attenuation for the two frequencies (rain attenuation at Ka is approximately from two to six times larger than at Ku, compare the values corresponding to the black lines in the top two panels on the left). Note also the better sensitivity of the Ku against the matched scan Ka. Despite the lower sensitivity, it must be kept in mind that the DPR, with its 245 km swath, does provide a full 3D view of the storm and not simply a curtain through it like the CPR. This case study epitomizes the complementarity of these systems (Battaglia et al., 2020a). Luo et al. (2017) exploited the TRMM and CloudSat matchups (with the co-located measurements of Cloud-Aerosol Lidar and Infrared Pathfinder Observation, CALIPSO) to study tropical cloud and precipitation regimes and their internal vertical structures. Berg et al. (2010) combined the TRMM-PR and the CloudSat CPR, best positioned to detect and quantify the high/medium and drizzle/light

10.1002/9781119700357.ch15, Downloaded from https://agupubs.onlinelibrary.wiley.com/doi/10.1002/9781119700357.ch15 by Maki Kikuchi - Cochrane Japan , Wiley Online Library on [21/12/2023]. See the Terms and Conditions (https://onlinelibrary.wiley.com/terms-and-conditions) on Wiley Online Library for rules of use; OA articles are governed by the applicable Creative Commons License

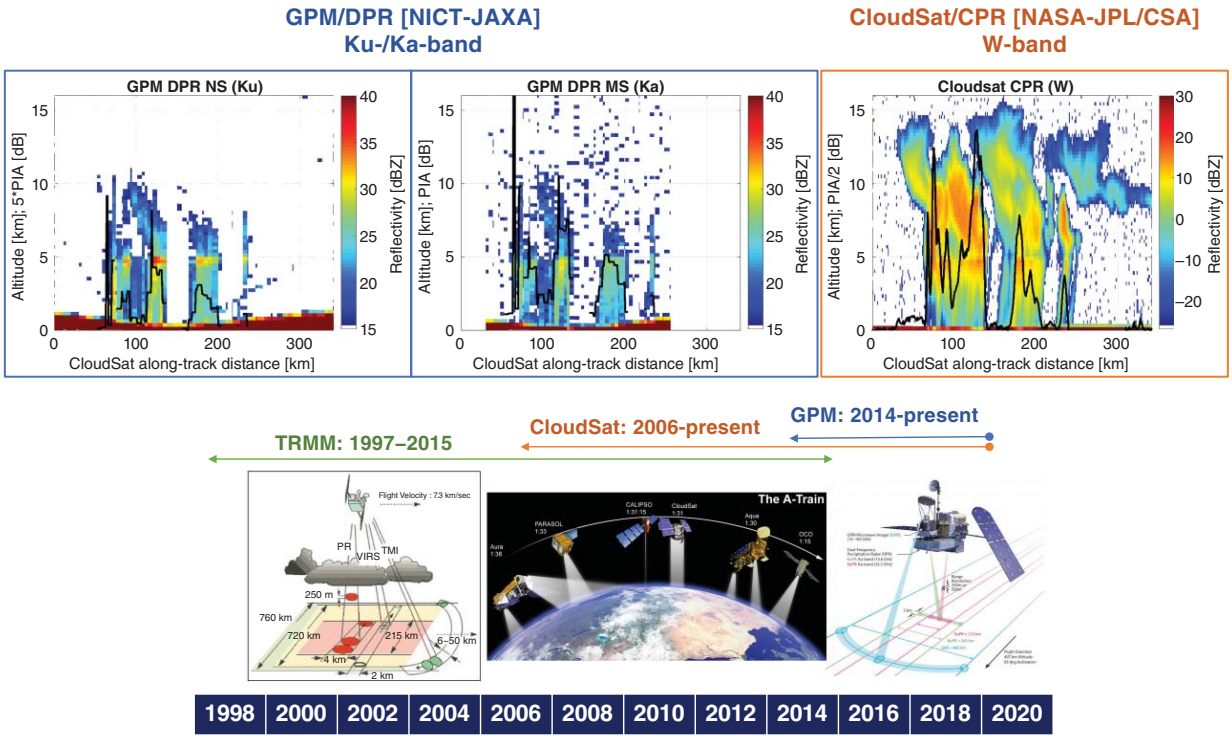

Figure 15.2 Timeline of active cloud and precipitation radar missions with, above, drawings of the TRMM PR scanning pattern, the CloudSat CPR A-Train constellation formation, and the GPM core satellite. The top three panels provide an example of the current space-borne cloud and precipitation radar capabilities with almost coincident vertical profile reflectivities of the GPM Ku (left panel), the GPM Ka (center panel), and the CloudSat W-band (right panel) corresponding to a precipitating systems observed on 4 June 2014. The over plotted black lines (with scaling factors as indicated in the y-labels) indicate the path integrated attenuation as derived from surface reference techniques. The case study is from the GPM product 2B-CSATGPM. Source: NASA / Public Domain.

10.1002/9781119700357.ch15, Downloaded from https://agupubs.onlinelibrary.wiley.com/doi/10.1002/9781119700357.ch15 by Maki Kikuchi - Cochrane Japan , Wiley Online Library on [21/12/2023]. See the Terms and Conditions (https://onlinelibrary.wiley.com/terms-and-conditions) on Wiley Online Library for rules of use; OA articles are governed by the applicable Creative Commons License

rain, respectively, to provide the best estimates of the total rain volume in the tropical oceans.

Reflectivity profiles like those shown in Figure 15.2 are used to derive microphysical profiles of hydrometeors. A list and details of TRMM, CloudSat, and GPM products can be found at https://gpm.nasa.gov/data/directory, www.cloudsat.cira.colostate.edu/data-products, and https://gportal.jaxa.jp/gpr/, respectively. There are three fundamental issues when converting the measured radar range-resolved quantities into precipitation profiles:

1. ambiguities in the effective radar reflectivity factors versus precipitation rates conversion which are related to the natural variability of the particle size distribution and, for solid precipitation, of the particle shapes and densities;
2. the attenuation correction required to derive the effective radar reflectivity factors from the measured reflectivity factors. Rain attenuation is increasingly important with increasing frequency and precipitation rate; graupel and snow may produce non-negligible attenuation already at Ka and W bands (Lhermitte, 1990);
3. non-uniform beam filling (Nakamura, 1991) and multiple-scattering effects (Battaglia et al., 2010) that are more pronounced in the presence of large footprints and strongly attenuating media.

The first issue is generally addressed by adopting *a priori* assumptions on the particle size distribution shape (e.g., for rain in TRMM and GPM algorithms (Iguchi & Haddad, 2020) or for snow in the CloudSat 2C-snow algorithm (Wood & L'Ecuyer, 2013)); caution must be taken because such assumptions depend on precipitation regimes and may show regional biases (e.g., Protat et al., 2019). In fact, dual- and multi-frequency observations have been proposed for mitigating such uncertainties (Battaglia et al., 2020b; Iguchi & Haddad, 2020). The second issue, attenuation correction, is an essential step in all retrieval algorithms and is performed either via analytical solutions (Seto & Iguchi, 2015) or via optimal estimation-based iterative processes (L'Ecuyer & Stephens, 2002). Because errors in all of these techniques are accumulated recursively with increasing range (Hitschfeld & Bordan, 1954), additional constraints, such as the PIA estimated from the surface reference technique (Meneghini et al., 2015), are usually exploited in order to stabilize the retrieval. Finally, non-uniform beam filling corrections have been accounted for in TRMM and DPR algorithms (Seto et al., 2015), whereas multiple scattering is intrinsically accounted for when adopting appropriate forward models (e.g., Hogan & Battaglia, 2008) as in CloudSat rain products. However, there are instances associated with extreme events where the two effects occur simultaneously (Mroz et al., 2018); tackling both remains challenging and is topic of current research.

Despite the above issues, these radar measurements have mapped for the first time the global vertical distributions of clouds and precipitation. What is noteworthy is that the precipitation radars not only identified precipitation itself, but also gave observational insights into latent heating in the tropical atmosphere, including its diurnal, intraseasonal, seasonal, and annual variability, as well as its role in tropical and extratropical circulations (Simpson et al., 1988) (see also Chapter 10: Interactions Between the Tropical Atmospheric Overturning Circulation and Clouds in Present and Future Climates). One of the science drivers of the missions was the improvement of climate modeling and prediction, and the provision of precipitation microphysics and latent heat release were viewed as being needed to improve Earth system models (Hou et al., 2014). Studies have used the latent heating products to examine the response of atmospheric circulation to heating (Huaman & Schumacher, 2018; Mathew & Kumar, 2019; Schumacher et al., 2004), to describe the Madden-Julian Oscillation (MJO) (Barnes et al., 2015; Chang & L'Ecuyer, 2019; Vincent & Lane, 2018), and to characterize the contributions to latent heating of precipitation systems with different sizes, depths, and intensities (Liu et al., 2015).

Further, a number of recent studies employed the combinations of radar/radiometers to characterize the properties of hailstorms in an attempt to develop hail climatologies. For example, Marra et al. (2017) identified DPR and GMI properties for a severe hailstorm over Italy and placed it in the context of 2 years of GPM data. Mroz et al. (2018) examined the vertical structure of more than 800 hailstorms using DPR and noted particular features of Ka-band reflectivity profiles associated with hail, including multiple scattering and non-uniform beam filling. Bang and Cecil (2019) used 16 years of TRMM data to pair TMI brightness temperatures with surface hail reports and apply those relationships to GMI data to construct a near-global climatology of hail.

The precipitation measurements by these active radars and passive radiometers better shaped the distribution and properties of global precipitation. In light of this, more efforts were made in later years to understand coupled cloud-precipitation processes from the measurements and propose observation-based metrics in evaluating the representation of those processes in numerical models. The next section introduces examples of such process studies, attempting to reveal the mechanisms behind the precipitation phenomena identified.

15.4. UNDERSTANDING CLOUD-PRECIPITATION PROCESSES

Cloud-precipitation processes are central to the fundamental question with regard to atmospheric water:

10.1002/9781119700357.ch15, Downloaded from https://agupubs.onlinelibrary.wiley.com/doi/10.1002/9781119700357.ch15 by Maki Kikuchi - Cochrane Japan , Wiley Online Library on [21/12/2023]. See the Terms and Conditions (https://onlinelibrary.wiley.com/terms-and-conditions) on Wiley Online Library for rules of use; OA articles are governed by the applicable Creative Commons License

How does precipitation form from clouds? As should be obvious from this question, precipitation formation accompanies consecutive changes in physical properties of cloud and precipitating particles, and as such, there has been emerging recognition in the importance of analyzing both cloud and precipitation measurement simultaneously, rather than investigating cloud and precipitation formed separately. The following sections introduce selected example studies that analyzed active and passive measurements synergistically in an attempt to address this fundamental science question.

15.4.1. Warm Rain Processes

The unique capability of CloudSat CPR to vertically profile the cloud and light precipitation offered a novel opportunity to study rain formation processes, particularly when combined with passive measurements of clouds included in A-Train. Early studies that exploited the simultaneous measurement of cloud and light precipitation (e.g., Kubar et al., 2009; Leon et al., 2008; Wood et al., 2009) investigated how CloudSat-observed radar reflectivity relates to MODIS-derived cloud properties such as cloud top particle size, cloud optical depth, and liquid water path (LWP) to find that the radar reflectivity systematically varies with these cloud properties. The light precipitation measurement by CloudSat was also combined with aerosol information obtained from MODIS to assess how rain formation tends to be suppressed by increasing aerosols (Lebsock et al., 2008; L'Ecuyer et al., 2009; Wang et al., 2012). Specifically, these studies investigated probability of precipitation (POP) quantified by light precipitation measurement of CloudSat as a function of LWP from MODIS or AMSR-E for differing conditions of aerosol turbidity also characterized by MODIS. Aerosol impacts on precipitation were then assessed by analyzing how POP tends to increase with increasing LWP at a rate that differs depending on aerosol turbidity (measured by aerosol optical depth or aerosol index). The global statistics thus constructed depicted the aerosol impacts on the warm rain formation process. Wang et al. (2012) further extended this analysis to introduce the sensitivity or "susceptibility" of POP to perturbed aerosols, denoted by S_{pop} as an analog to the precipitation susceptibility S_p (Sorooshian et al., 2009), and showed that global models tend to overestimate S_{pop} relative to satellite observations, implying a too pronounced response of the cloud-precipitation system to perturbed aerosols in climate models.

The vertical profiling capability of CloudSat CPR was further exploited by some studies (e.g., Nakajima et al., 2010; Suzuki et al., 2010) to explore cloud-to-precipitation processes. These studies constructed particular statistics of CloudSat radar profiles rescaled by cloud optical depth and classified according to cloud top particle size obtained from MODIS to observationally "fingerprint" the cloud-to-precipitation processes. The statistics illustrated how vertical microphysical structures vary systematically from non-precipitating to precipitating characteristics as a fairly monotonic function of the cloud top particle size, and such a microphysical signature found in the statistics was interpreted in the context of drop collection process.

In light of such fingerprints from the analysis, subsequent studies have used these results to assess the credibility of cloud-precipitation processes in numerical models (such as climate models and cloud-resolving models). As in other satellite-based model evaluations, these studies employed satellite simulators that translate model geophysical parameters into satellite-observed radiances/backscatters (Bodas-Salcedo et al., 2011; Haynes et al., 2007; Hashino et al., 2013; Masunaga et al., 2010; Voors et al., 2007). As seen in section 15.3, each observation sensor has its own sensitivity/attenuation characteristics, as well as spatial and temporal resolutions. Consequently, comparing satellite measurements to model simulations requires these satellite characteristics to be taken into account, rather than comparing satellite measurements directly to native model outputs. These satellite simulator frameworks provide what a satellite would have measured if it flew over the modeled atmosphere. This reduces the ambiguities attributed to satellite measurement characteristics, enabling a more consistent "scale-aware and definition-aware" evaluations (Kay et al., 2018).

Model evaluations in this manner exposed that state-of-the-art global models, including cloud-resolving models and climate models, share a common propensity to produce rain even when the clouds consist of small droplets (Jing et al., 2017; Suzuki et al., 2011, 2015), as a key cause of the "too-light, too-frequent" precipitation bias in global models identified against satellite observations (Dai, 2006; Stephens et al., 2010). The model-satellite comparisons also offered a process-based constraint on key uncertainties of climate models that have typically been regarded as "tunable knobs". A threshold cloud particle size that triggers rain formation is one particular example for such a tuning parameter in climate models (Golaz et al., 2013). It is shown that the model assumption on this parameter that *best* represents the satellite-observed rain statistics leads to a historical temperature trend that provides the *worst* match to the observed trend and vice versa (Suzuki et al., 2013). This "dichotomy" between the process-based constraint and the top-down energy balance requirement is caused by the radiative forcing due to aerosol-cloud interaction that is too large and negative such that it cancels much of the global warming in twentieth century,

10.1002/9781119700357.ch15, Downloaded from https://agupubs.onlinelibrary.wiley.com/doi/10.1002/9781119700357.ch15 by Maki Kikuchi - Cochrane Japan , Wiley Online Library on [21/12/2023]. See the Terms and Conditions (https://onlinelibrary.wiley.com/terms-and-conditions) on Wiley Online Library for rules of use; OA articles are governed by the applicable Creative Commons License

as a result of pronounced cloud responses to aerosols enhanced by wet-scavenging of aerosols (Jing & Suzuki, 2018; Jing et al., 2019). This underscores a critical need for better modeling the aerosol-cloud-precipitation coupling.

These studies imply the presence of error compensations in modern climate models, which need to be mitigated for enhancing model reliability of climate projections. The process-based analysis of satellite observations such as those described above also can serve as a guide to improve the models at a fundamental process level. Recently, Michibata and Suzuki (2020) demonstrated that a sophisticated prognostic precipitation parameterization in a climate model can reconcile the error compensation described above to simultaneously represent both rain processes consistent with satellite observations and reasonable magnitudes of radiative forcing due to aerosol-cloud interaction (Fig. 15.3). This highlights how satellite measurement of warm-rain process can be exploited to advance climate modeling (Stephens et al., 2019b) and underscores that such a process-oriented effort in combining models and satellite observations should be extended to understanding of the cold-rain processes, which is another source of uncertainty in climate projections.

15.4.2. Mixed-phase Cloud and Snowfall Processes

Mixed-phase clouds are ubiquitous globally in temperature conditions between 0°C and –40°C. Commonly found in the Southern Ocean and Arctic are ice clouds with thin supercooled liquids at the cloud top and snow falling out near the ground (Morrison et al., 2012; Shupe, 2011). This three-layered structure has been observed using CloudSat CPR with the CALIPSO's scattering lidar, Cloud-Aerosol Lidar with Orthogonal Polarization (CALIOP). The constellation formation of the CloudSat and CALIPSO captures the cloud-precipitation structure almost simultaneously, where the CALIPSO lidar observes the liquid layer at the top and the CloudSat radar observes the ice cloud and snowfall underneath (Forbes & Ahlgrimm, 2014; Huang et al., 2012). According to ground-based observations, the structure often persists for several days (Shupe, 2011), which is relatively unexpected given that the coexistence of liquid and ice is microphysically unstable. Whenever ice and liquid water exist in subfreezing temperatures, the WBF process enhances the evaporation of liquid droplets into water vapor, which are then condensed onto ice, meaning the process supports ice growth at the expense of neighboring liquid droplets (c.f. section 15.1). As such, the microphysical instability can transit mixed-phase clouds into all-iced clouds in a short period of time and the persistence of these clouds for several days is quite surprising. Still, the supercooled liquid layer lasts, suggesting a strong liquid condensation at the cloud top with continuous supply of water vapor that balance continuous liquid mass-loss by ice growth and precipitation. Although not fully understood, the preserving processes involves cloud-scale upward air motion (acting to increase relative humidity), radiative cooling at the cloud top (acting to decrease the static stability and thus driving turbulence), and large-scale advection of water vapor near the cloud top (Morrison et al., 2012).

The complexity of mixed-phase clouds in association with local processes as exemplified above gives rise to fundamental challenges for representing them in global climate and weather prediction models. In particular, it has been recognized as a longstanding mixed-phase cloud problem within the climate modeling community that models tend to underestimate supercooled liquid clouds over the Southern Ocean and (to a lesser extent) in the Arctic (Bodas-Salcedo et al., 2012, 2014, 2016; Kay et al., 2016; Kawai et al., 2019; Trenberth & Fasullo, 2010). In general, for a given cloud water content, cloud liquid droplets are much smaller than cloud ice crystals, which leads liquid clouds to become optically thicker and reflect more solar radiation than ice clouds (Cesana & Storelvmo, 2017). As such, the lack of supercooled water over the regions induces the models to absorb excessive solar radiation and overestimate sea surface temperature (SST). For example, McIlhattan et al. (2017) found the insufficient liquid in Arctic clouds in the climate model of the Community Earth System Model Large Ensemble (CESM-LE), and, in turn, generates too much snowfall than what CloudSat precipitation measurements suggested. They speculated that the WBF process in the model was progressing too fast, contributing in part to scavenging the liquid clouds too efficiently. Recognizing the substantial impacts on cloud-precipitation-ocean-radiation processes (Kay et al., 2016), a number of studies in recent years worked on reducing the supercooled liquid deficit by adjusting phase partitioning of clouds in the model, essentially slowing cloud freezing processes and sustaining more liquids in clouds (e.g., Forbes et al., 2016).

The changes in the phase partitioning subsequently exert profound impact on future climate projections since the melting of cloud ice to liquid in a warming climate increases cloud albedo and thereby induces a negative cloud phase feedback onto the climate (Storelvmo et al., 2015). Tan et al. (2016) illustrated this using the National Center for Atmospheric Research's Community Atmosphere Model (CAM) model by adjusting cloud phase partitioning in the models to what satellite observations implied. They found that the adjustment decreased cloud glaciation rate in a warmer climate that weakened the negative feedback and induced higher climate sensitivity. The follow-up work by Tan and Storelvmo (2019)

10.1002/9781119700357.ch15, Downloaded from https://agupubs.onlinelibrary.wiley.com/doi/10.1002/9781119700357.ch15 by Maki Kikuchi - Cochrane Japan , Wiley Online Library on [21/12/2023]. See the Terms and Conditions (https://onlinelibrary.wiley.com/terms-and-conditions) on Wiley Online Library for rules of use; OA articles are governed by the applicable Creative Commons License

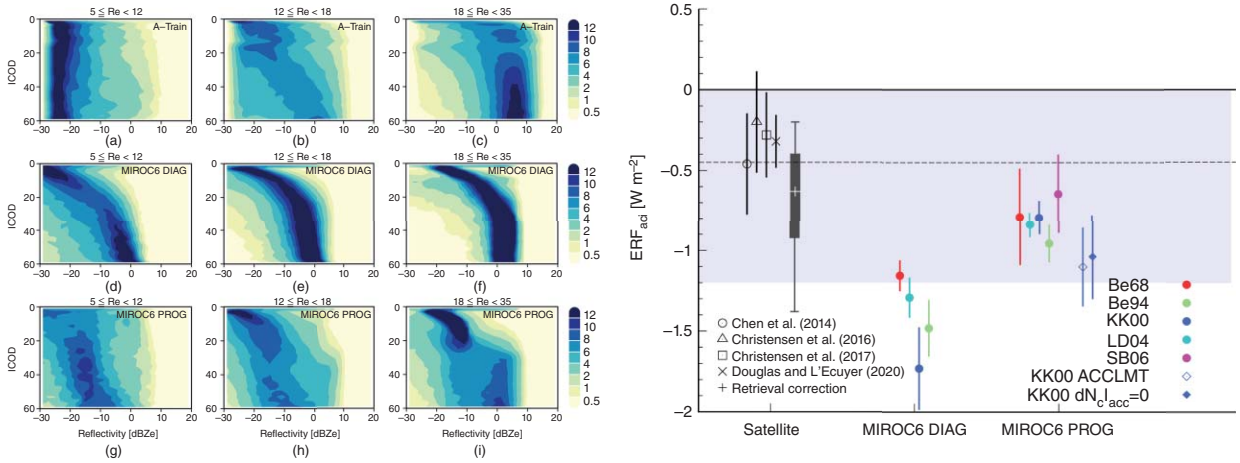

Figure 15.3 (Left) Statistical representations of radar reflectivity profile as a function of in-cloud optical depth (ICOD) classified according to cloud top particle size (Re) from (top) A-Train, (middle) MIROC6 old version, and (bottom) MIROC6 new version. (Right) Effective radiative forcing due to aerosol-cloud interaction estimated by satellite and two versions of MIROC6. Source: Michibata et al. (2020) / John Wiley & Sons/ Public Domain.

10.1002/9781119700357.ch15, Downloaded from https://agupubs.onlinelibrary.wiley.com/doi/10.1002/9781119700357.ch15 by Maki Kikuchi - Cochrane Japan , Wiley Online Library on [21/12/2023]. See the Terms and Conditions (https://onlinelibrary.wiley.com/terms-and-conditions) on Wiley Online Library for rules of use; OA articles are governed by the applicable Creative Commons License

interestingly explained the contradicting effects of the cloud phase change on the faster warming of the Arctic compared to the rest of the globe – commonly referred to as the "Arctic amplification." They showed that the cloud phase change during a warming atmosphere initially *reduces* the warming by the negative cloud phase feedback, but at the same time could ultimately *enhance* the Arctic amplification by increase in downward longwave radiation trapped by the prolonged clouds as a result of the smaller liquid droplets (than ice clouds) that produce less precipitation.

The studies above underscored the importance of realistic representation of mixed-phase cloud-to-precipitation processes in the models. Some studies compared the models against CloudSat measurements to find that the models generally produce snowfall too frequently (Kay et al., 2018; Palerme et al., 2017). In an attempt to mitigate this bias, Reitter et al. (2011) introduced a prognostic precipitation scheme that interacts with cloud and ambient environment during sedimentation, instead of the conventional diagnostic scheme with no such interaction. Since snow falls out instantaneously in the diagnostic scheme, the authors found considerable underestimates of the large ice water content (IWC) compared to CloudSat, while the prognostic scheme resulted in overestimates of IWC with the excess ice clouds remained in the atmosphere due to the insufficient snow fall speed, as also suggested by comparison with CloudSat. More recently, Michibata et al. (2019) also introduced a prognostic precipitation scheme in another climate model to achieve better agreement with CloudSat/CALIPSO in total cloud ice content and showed a substantial radiative impact by falling snow of 6.4 W/m^2 in longwave and 5.1 W/m^2 in shortwave.

The mixed-phase clouds and ice precipitation also have profound influences on the polar ice sheet through radiation and snowfall. This is particularly important in the context of evolving mass budget of the Arctic ice sheet with its substantial impact on sea level rise. Boening et al. (2012) used the CloudSat snowfall observations (with the ERA Interim reanalysis) and showed the significant mass increase during 2009–2011 observed by satellite gravitational measurements of Gravity Recovery and Climate Experiment (GRACE) was caused by extreme precipitation events during the austral winter. Palerme et al. (2017) showed that the models in the Fifth Climate Model Intercomparison Project (CMIP5) archive generally predict increases in the Antarctic precipitation (from 5.5% to 24.5%) between the periods 1986–2005 and 2080–2099, with the subset models in agreement with CloudSat snowfall (within 20% of error) estimating larger increases (from 7.4% to 29.3%) implying larger impacts on sea level rise. This underscores a critical role of satellite precipitation measurement in evaluating the processes controlling sensitive balance between the snowfall accumulation and glacial discharge, and their impact on sea level rise in a warming climate. Despite these attempts, process-level understandings of mixed-phase precipitation have generally not yet advanced as much as of warm-rain processes due to the microphysical complexity of ice and snow hydrometeors. This called for ice and mixed-phase processes to be one of the major scientific questions in future missions as highlighted in section 15.5.

15.4.3. Latent Heat and Convective Processes

The latent heat released during precipitation formation is a fundamental factor in atmospheric circulation and convective storm evolution. Stephens et al. (2019a) emphasizes analyzing simultaneous measurements of cloud and precipitation with a focus on the radiative and latent heating characteristics related to different cloud-precipitation vertical structures. They employed CloudSat cloud and precipitation observations combined with GPM precipitation, CALIPSO lidar, and MODIS radiance data to investigate the cloud properties of precipitation. They considered two cloud top height (CTH) parameters, the maximum or highest CTH (designated HCTH), typical of what might be estimated from radiometric observations, and the lowest CTH of the raining column (designated RCTH) derived from an active instrument capable of detecting overlapping cloud layers. Not too surprisingly, they found that HCTH, indicative of the deepest raining clouds in the tropics, was a poor gauge of rainfall intensity and led to misclassification of rainfall associated with shallower cloud systems overtopped by higher clouds. For HCTH, precipitation was associated with a bimodal distribution of CTHs, with rain appearing to occur primarily with deeper convective cloud systems and shallow, primarily subtropical clouds. For RCTH, the proportion of rainfall from deeper systems was reduced, while rainfall from shallow and congestus systems increased, with the CTH distribution exhibiting more of a trimodal nature of shallow, midlevel, and deep systems.

Using a clustering methodology, they identified three main modes of organization: a deep, optically thick mode associated with deep convection; a deep, optically thin (designated "mixed") mode; and a shallow mode representing shallow convection and stratiform precipitation. The mixed mode consisted of shallow to deep precipitating clouds underneath high clouds for the HCTH distribution and deep, but optically thinner clouds for RCTH. Stephens et al. (2019a) showed that for the RCTH distribution, the shallow/mixed/deep modes made the largest/middle/least contributions to light rainfall (<1 mm hr^{-1}), with the reverse true for heavy (>10 mm h^{-1}) rainfall. They also related these cloud

10.1002/9781119700357.ch15, Downloaded from https://agupubs.onlinelibrary.wiley.com/doi/10.1002/9781119700357.ch15 by Maki Kikuchi - Cochrane Japan , Wiley Online Library on [21/12/2023]. See the Terms and Conditions (https://onlinelibrary.wiley.com/terms-and-conditions) on Wiley Online Library for rules of use; OA articles are governed by the applicable Creative Commons License

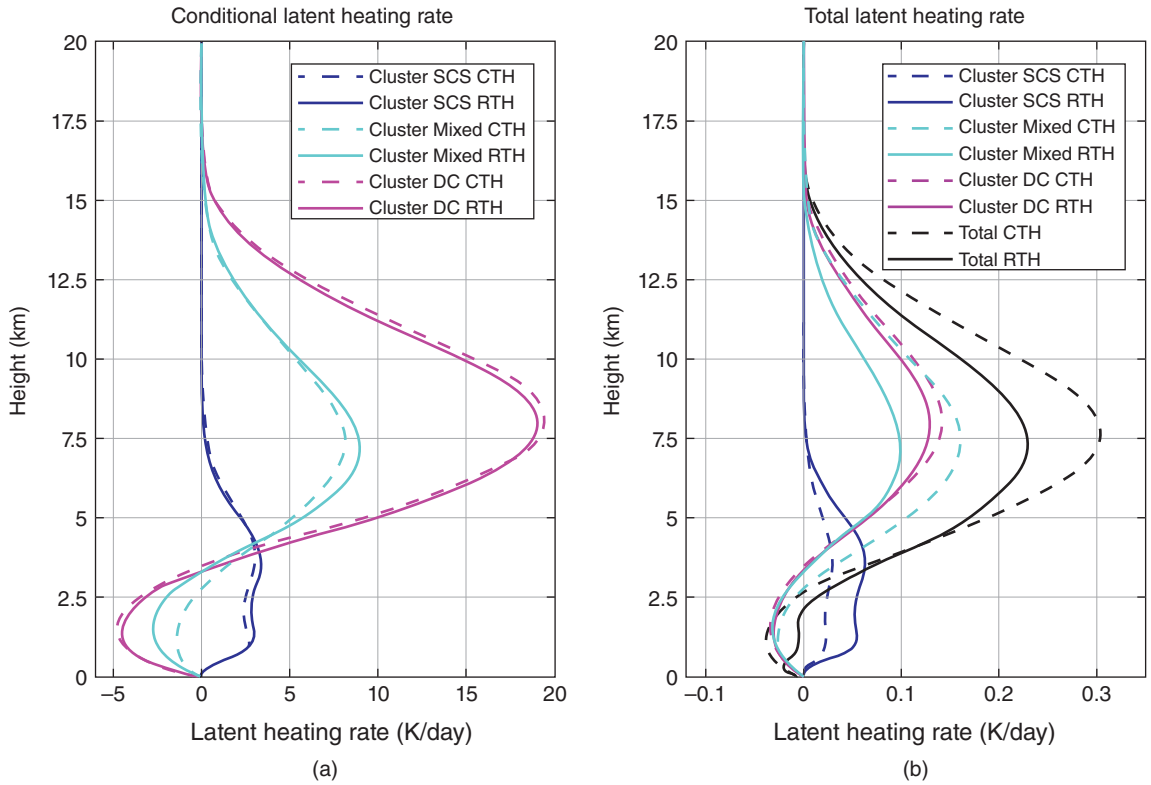

Figure 15.4 (a) The conditional profile latent heating averaged over the tropics when precipitation occurs. (b) The equivalent profiles weighted by the occurrence of each k-means cloud regime, interpreted as the total latent heat contribution from oceanic raining clouds to the total tropical atmosphere. Source: Stephens et al. (2019) / John Wiley & Sons.

modes to latent heating rate profiles (Fig. 15.4) derived from the approach of Schumacher et al. (2004). Averaged heating rates (Fig. 15.4a, conditioned on when precipitation occurs) were similar for the HCTH and RCTH datasets. Latent heating rates for deep systems exhibited a top-heavy profile typical of deep convective systems (convective and stratiform regions). The mixed mode had a similar shape, but with smaller heating/cooling rates, while the shallow mode was characterized by heating up to 7.5 km altitude. When weighted by the frequency of occurrence of the different modes (Fig. 15.4b), the heating rates exhibited more sensitivity to the measure of CTH, with slightly reduced deep-mode heating and substantially reduced mixed-mode heating aloft and increased shallow heating at lower-to-middle levels. Thus, the shallow mode plays a greater role when the more realistic treatment of CTH is used, with the shallow heating largely cancelling the cooling from the deep and mixed modes at low levels.

Huaman and Schumacher (2018) examined the relationship between the distribution of latent heating in the eastern Pacific intertropical convergence zone (ITCZ) and the meridional circulation that it drives. They calculated latent heating rates using an approach similar to Schumacher et al. (2004) in which heating from convective and stratiform precipitation regions was derived from TRMM rainfall rates and heating from lighter shallow precipitation was estimated from CloudSat data. While Huaman and Schumacher (2018) discussed all seasons, only results for June-July-August (JJA) are shown here (Fig. 15.5a). They found distinct seasonal variability, with the northern ITCZ strongest in JJA, with a low- and high-level heating peak. The first six months of the year, in contrast, were characterized by a low-level peak near 800–700 hPa. Other than March-April-May, the southern ITCZ was associated with shallow heating only, with a peak just below 800 hPa. Huaman and Schumacher (2018) also noted that the northern ITCZ sloped northward with height due to a predominance of shallow (deep) heating on its southern (northern) side. Average latent heating rates in the ITCZ (Fig. 15.5b) showed considerable variability between the different estimates. The two TRMM/GPM standard products (CSH and SLH) were reasonably similar, with a top-heavy heating profile peaking near 400 hPa. While the Huaman and Schumacher PR-CPR latent heating profile was similar

10.1002/9781119700357.ch15, Downloaded from https://agupubs.onlinelibrary.wiley.com/doi/10.1002/9781119700357.ch15 by Maki Kikuchi - Cochrane Japan , Wiley Online Library on [21/12/2023]. See the Terms and Conditions (https://onlinelibrary.wiley.com/terms-and-conditions) on Wiley Online Library for rules of use; OA articles are governed by the applicable Creative Commons License

to CSH and SLH above 500 hPa, it showed a distinct low-level heating peak near 700 hPa associated with the CPR estimates of shallow-cloud heating.

Huaman and Schumacher (2018) compared the satellite-derived heating rates to vertical motions and circulation vectors from two reanalysis datasets of the Modern-Era Retrospective analysis for Research and Applications, version 2 (MERRA2; Fig. 15.5c), and the National Centers for Environmental Prediction–the National Center for Atmospheric Research reanalysis (NCEP-NCAR reanalysis; Fig. 15.5d). The patterns of vertical velocity were consistent with the heating rates, with the largest differences between reanalyses occurring in the JJA and September-October-November (SON) timeframes. The deep, top-heavy heating profile produced a deep overturning circulation, while the low-level heating peak gave rise to a shallow meridional overturning circulation. While not as apparent during JJA, the shallow circulation was apparent in the MERRA2 data (southerly flow in the 800–700 hPa layer, Fig. 15.5c), but was absent in the NCEP-NCAR reanalysis (Fig. 15.5d), which had only weak shallow heating. Their results suggest potentially significant issues with the representation of organized convection and shallow clouds in global circulation models.

The latent heat released during cloud condensation and precipitation formation warms the air and enhances instability inside clouds in adiabatic conditions that invigorates the storms. Deep convective storms are a key source of intense precipitation. The linkage between convection and extreme precipitation has been investigated using the precipitation radars of TRMM and DPR (Gingrey et al., 2018: Kuo et al., 2020; Sohn et al., 2013; Wang & Tang, 2020). Extreme rainfall events were studied by Hamada et al. (2015) using long-term TRMM PR data record. Interestingly, they showed that extreme rainfall events associated with deep convective clouds tend to *not* be associated with extremely tall convective systems. This is illustrated in Figure 15.6 as a statistical difference in vertical profiles of PR-observed radar reflectivity between extreme rainfall and convection cases. A remarkable finding is a downward increase of reflectivity below 8 km in the extreme rainfall ("R-only") case, indicative of a substantial contribution of the warm rain process to formation of the extreme rainfall. The extremely tall ("H-only") case, in contrast, is characterized by more vertically aligned structures even with a slight downward decrease of reflectivity below the melting level. This difference in occurrences between the extreme rainfall and convection cases highlights a critical need for understanding

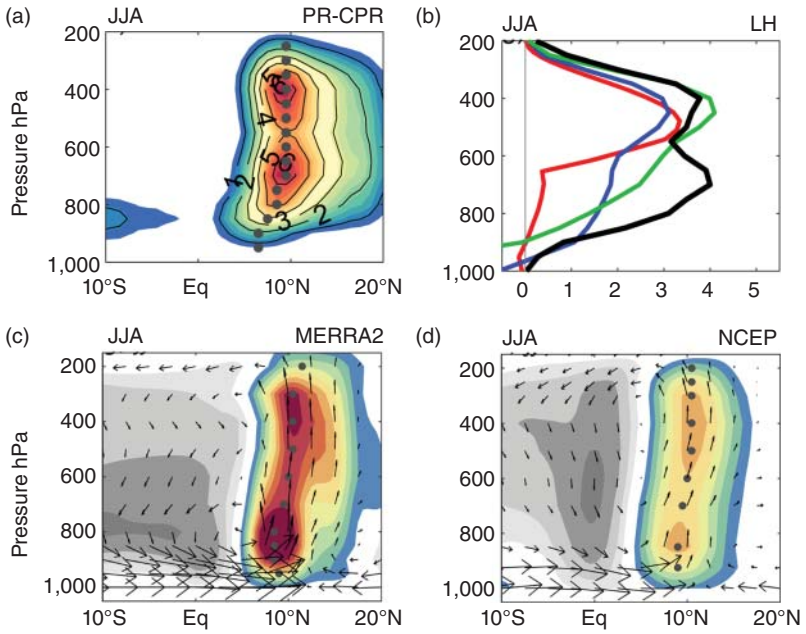

Figure 15.5 (a) Mean latitude-pressure cross-section of latent heating (K day-1) for June-July-August for 130°–90°W from the CloudSat CPR and TRMM PR. (b) Latent heating profiles in the ITCZ (region of precipitation >3 mm day^{-1}) derived from TRMM/CloudSat (black) and TRMM PR-based retrievals: CSH (green), SLH (blue), and PRH (red). (c)–(d) Mean meridional mass flux vectors (kg m^{-2}s^{-1}) and vertical velocity (Pa s^{-1}; shaded) from (c) MERRA-2 and (d) and NCEP-NCAR. The vertical flux component has been amplified 100 times to account for the aspect ratio of the plot. The maximum heating position at each level in (a, c, and d) is indicated by gray dots. Source: Huaman et al. (2018) / with permission of American Meteorological Society.

10.1002/9781119700357.ch15, Downloaded from https://agupubs.onlinelibrary.wiley.com/doi/10.1002/9781119700357.ch15 by Maki Kikuchi - Cochrane Japan , Wiley Online Library on [21/12/2023]. See the Terms and Conditions (https://onlinelibrary.wiley.com/terms-and-conditions) on Wiley Online Library for rules of use; OA articles are governed by the applicable Creative Commons License

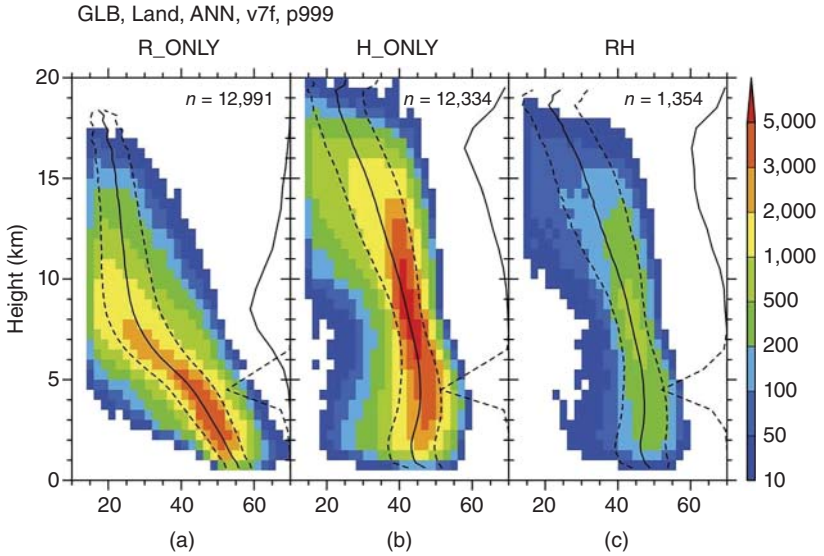

Figure 15.6 Vertical profiles of radar reflectivity statistically represented in the form of joint histograms of radar reflectivity and height over tropical ocean for extreme rainfall (R-only), extreme vertical extent (H-only), and extreme relative humidity (RH) cases. Source: Hamada et al. (2015) / Springer Nature / CC BY 4.0.

relative roles of microphysical and dynamical processes in cloud-precipitation systems. Although the two different aspects (i.e., microphysics and dynamics) have started to be linked with some combinations of active and passive sensors for a spectrum of shallow to deep convective systems (e.g., Kikuchi & Suzuki, 2019), their process-level understanding is still generally missing. Chapter 14: Observed Scaling of Precipitation Extremes discusses dependence of these extreme events on both surface temperature and atmospheric instability in more detail.

15.4.4. Tracking Temporal Evolution

Strictly speaking, the term "process" means the mechanisms responsible for *temporal* evolution of physical states (as discussed in section 15.1). In this sense, the analysis discussed above in this section just "probe" processes statistically, rather than readily "seeing" processes, with a lack of *time* dimension in the analysis. These statistical probing processes are mainly due to the limitation of low Earth orbiting satellites that sample clouds and precipitation only intermittently at a given location and the fact that temporally continuous measurements enabled by recent geostationary satellites (e.g., Himawari-8 and GOES-R) have neither cloud nor precipitation radars onboard. Despite this limitation, however, there have been several attempts to extract "temporal" information of cloud-precipitation system from existing satellite measurements (Fiolleau & Roca, 2013; Letu et al., 2019; Wardah et al., 2008). One such approach is proposed by Luo et al. (2009, 2010) who combined cloud-precipitation states measured by A-Train multi-sensor satellites with information on the ambient environment to infer dynamical characteristics of deep convective clouds, such as whether a given convective system is "transient" or "terminal" in terms of its buoyancy (Luo et al., 2009) and an estimate of the cloud top buoyancy and entrainment rate (Luo et al., 2010). Along with these "indirect" approaches, a more "direct" approach to infer cloud top dynamics is proposed by Luo et al. (2014), who suggested the use of A-Train multiple satellite measurements (i.e., Aqua/MODIS and CALIPSO/IIR) with a slight time lag (~1–2 minutes). They derived convective vertical velocities by taking a difference in cloud top temperatures (measured by the IR channels on both satellites) and related them to cloud internal structures inferred from the CloudSat profiles, thus bringing together cloud dynamics and cloud microphysics. These A-Train analyses are also combined with geostationary satellite measurements to put the cloud dynamic characteristics into the context of cloud life cycle (Takahashi & Luo, 2014).

Such time differences in multiple satellite measurements are also utilized in different and novel ways by Masunaga (2012), who analyzed data from multiple satellite platforms that overpass a given location at *different* local times to construct temporal composites of the satellite observables, often referred to as "*delta-t*" measurements. Specifically, Masunaga (2012) exploited the temporal gap between TRMM and Aqua satellite overpasses to project their measurements onto a composite temporal

10.1002/9781119700357.ch15, Downloaded from https://agupubs.onlinelibrary.wiley.com/doi/10.1002/9781119700357.ch15 by Maki Kikuchi - Cochrane Japan , Wiley Online Library on [21/12/2023]. See the Terms and Conditions (https://onlinelibrary.wiley.com/terms-and-conditions) on Wiley Online Library for rules of use; OA articles are governed by the applicable Creative Commons License

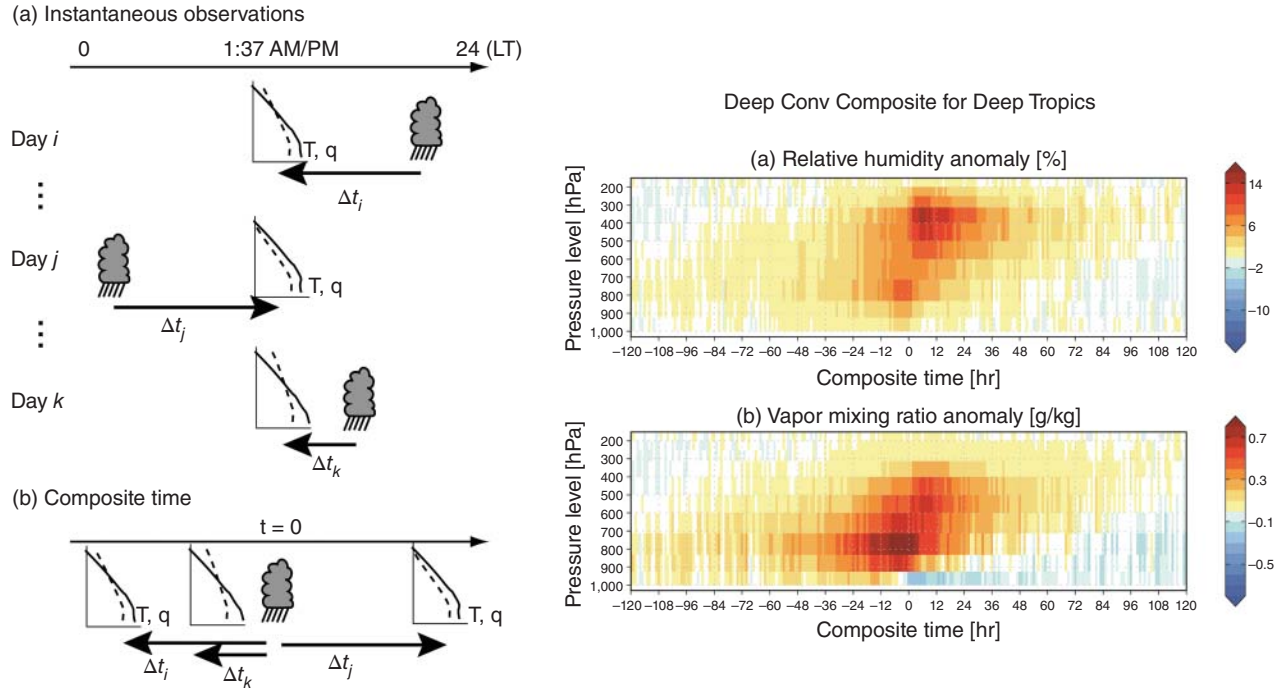

Figure 15.7 (Left) Schematic illustrations of the temporal composite analysis with (a) TRMM and Aqua measurements on individual days and (b) their projections onto the composite space. (Right) Temporal sequence of relative humidity anomaly (upper) and vapor mixing ratio anomaly (lower) composited with respect to deep convection. Source: Masunaga et al. (2012) / with permission of American Meteorological Society.

sequence of, for instance, water vapor mixing ratio as a function of relative time prior and subsequent to precipitation occurrence (Fig. 15.7, left panels), depicting temporal evolutions of water vapor profile associated with precipitating convection (Fig. 15.7, right panels). This analysis methodology was then applied to a variety of satellite platforms and sensors to investigate thermodynamic evolution of atmospheric phenomena relevant to convection and precipitation in the tropics and subtropics over relatively short (hourly to daily) timescales (e.g., Masunaga, 2013; Masunaga & Bony, 2018). This work exemplifies a promising approach to further advance our understanding of "dynamical" characteristics of cloud-precipitation processes, when combined with independent approaches of diagnosing cloud top dynamics described above (Luo et al., 2010, 2014) to infer convective and large-scale mass fluxes separately (Masunaga & Luo, 2016) and also through being applied to investigation of aerosol scavenging by convection (Sauter & L'Ecuyer, 2017; Sauter et al., 2019). These analysis approaches readily add the *time* dimension to satellite observations of cloud-precipitation systems and their interactions with aerosols and convection, particularly expected by the enhanced capabilities in future missions.

15.5. FUTURE SATELLITE MISSIONS FOR CLOUD-PRECIPITATION PROCESS STUDIES

The next radar mission, the Earth, Clouds, Aerosols and Radiation Explorer (EarthCARE) satellite, is developed jointly by the European Space Agency (ESA), JAXA, and National Institute of Information and Communications (NICT). EarthCARE is regarded as a historical successor of the vertical cloud and aerosol observations by the A-Train satellites, loading four sensors, (1) Cloud Profiling Radar (CPR), (2) Atmospheric Lidar (ATLID), (3) Multispectral Imager (MSI), and (4) Broadband Radiometer (BBR), all of which are specifically designed to investigate global profiles of cloud, aerosol, and precipitation and associated radiative properties (Illingworth et al., 2015). In terms of the precipitating cloud measurement, the EarthCARE CPR is expected to be the first space-borne weather radar with a Doppler measurement capability, enabling the measurement of vertical motions of hydrometeors globally (Kollias et al., 2014; Hagihara et al., 2021). Together with the High Spectral Resolution Lidar (HSRL) of ATLID, the measurements will offer novel information, that is, cloud dynamics and better particle habit identifications,

10.1002/9781119700357.ch15, Downloaded from https://agupubs.onlinelibrary.wiley.com/doi/10.1002/9781119700357.ch15 by Maki Kikuchi - Cochrane Japan , Wiley Online Library on [21/12/2023]. See the Terms and Conditions (https://onlinelibrary.wiley.com/terms-and-conditions) on Wiley Online Library for rules of use; OA articles are governed by the applicable Creative Commons License

to enhance our understanding on the precipitation processes described in previous sections particularly for mixed-phase clouds with cold rain processes, which had been challenging for previous measurements. In particular, the dynamical information offered by the CPR Doppler measurement is expected to add a temporal context to the cloud-precipitation vertical measurement achieved by the CloudSat.

With a particular focus in observing storm life cycles, the Time-Resolved Observations of Precipitation structure and storm Intensity with a Constellation of Smallsats (TROPICS) was selected by NASA as part of the Earth Venture-Instrument (EVI-3) program (Blackwell et al., 2018). The mission, led by the Massachusetts Institute of Technology/Lincoln Lab, was designed to obtain rapid-revisit passive microwave observations of tropical cyclones, with median revisit rates of less than 50 minutes. TROPICS comprises a constellation of four Cubesats, two satellites in each of two 30°-inclination orbits, each satellite carrying a passive microwave sensor with seven channels near 118 GHz for temperature profiling, three channels near 183 GHz for moisture profiling, and imaging channels at 92 and 205 GHz (Note that it originally planned for six satellites across three orbits, but the launch of the first two satellites failed to achieve orbit, thereby reducing the mean revisit rate to about 60 minutes). Its science objectives are focused on relating the evolution of precipitation structure, including convective bursts, to storm intensity change and warm-core development, relating environmental moisture to storm structure (including size) and intensity, and assessing the impact of the observations on numerical and statistical tropical cyclone prediction models.

Another promising observing system currently under formulation at NASA is the Atmosphere Observing System (AOS, https://aos.gsfc.nasa.gov), representing two designated observables identified in the 2017 Earth Science Decadal Survey (National Academies of Science, Engineering, and Medicine, 2018). The Aerosol designated observable focuses on vertical profiles of aerosol and clouds, with a candidate payload including a backscatter lidar and multi-channel, multi-angle, polarization imaging radiometer. For Clouds, Convection, and Precipitation (CCP), the science focuses on coupled cloud-precipitation properties and dynamics, with a candidate measurement approach that includes a possible dual-frequency Doppler radar with a multi-frequency passive microwave and sub-millimeter radiometer. The overall science objectives of AOS are defined to address diverse research objectives, including low- and high-cloud feedbacks; the dynamics of convective storm systems; cold cloud and precipitation processes (including snowfall and mixed-phase properties); aerosol attribution and air quality; aerosol processing, wet removal, and vertical redistribution; aerosol direct effects and absorption; and aerosol indirect effects. The architecture under formulation includes the candidate sensors identified above as well as important international contributions focused on convection and precipitation, the properties of ice clouds, and profiles of aerosols and moisture in the upper troposphere and lower stratosphere.

15.6. SUMMARY

Over the course of 50 years, satellite passive microwave instruments have provided unprecedented measurements for characterizing global precipitation. The measurement was essentially initiated by the microwave radiometer of SSM/I, which estimated precipitation using the microwave emission and scattering nature of hydrometeors. The successful continuity of microwave radiometry – including TRMM TMI, the AMSR series, SSMIS, and GPM GMI – established them as the backbone of the global precipitation satellite observing system. The first microwave radar measurements, acquired late in the twentieth century by the TRMM PR, added a vertical dimension to the 2D picture provided by the radiometers. Given the intrinsic 3D nature of cloud and precipitation systems, the measurements from the TRMM, CloudSat, and GPM radars accelerated process studies in the satellite community, looking deeper into physical mechanisms behind the precipitation observed. Such studies have shed light on key processes such as latent heat release, warm rain, and convective storm processes, and have even explored extracting temporal information from the snapshot observations. The "golden era" of satellite observations will be further nurtured by the planned EarthCARE mission and AOS observing system currently under study, with their enhanced capabilities that will further add a temporal dimension to global precipitation measurements and thus deepen our understanding of cloud-precipitation dynamics and their feedback mechanisms.

REFERENCES

Adler, R. F., & Negri, A. J. (1988). A satellite infrared technique to estimate tropical convective and stratiform rainfall. *Journal of Applied Meteorology and Climatology*, *27*, 30–51. https://doi.org/10.1175/1520-0450(1988)027<0030:ASITTE>2.0CO;2

Aonashi, K., & Ferraro, R. R. (2020). Microwave sensors, imagers and sounders. In V. Levizzani, C. Kidd, D. B. Kirschbaum, C. D. Kummerow, K. Nakamura, & F. J. Turk (Eds.), *Satellite precipitation measurement, advances in global change research* (Vol. 67, pp. 63–81). Cham: Springer. https://doi.org/10.1007/978-3-030-24568-9_4

10.1002/9781119700357.ch15, Downloaded from https://agupubs.onlinelibrary.wiley.com/doi/10.1002/9781119700357.ch15 by Maki Kikuchi - Cochrane Japan , Wiley Online Library on [21/12/2023]. See the Terms and Conditions (https://onlinelibrary.wiley.com/terms-and-conditions) on Wiley Online Library for rules of use; OA articles are governed by the applicable Creative Commons License

Arkin, P. A., & Meisner, B. N. (1987). The relationship between large-scale convective rainfall and cold cloud over the Western Hemisphere during 1982–84. *Monthly Weather Review*, *115*, 51–74. https://doi.org/10.1175/1520-0493(1987)115<0051:TRBLSC>2.0.CO;2

Ba, M. B., & Gruber, A. (2001). GOES multispectral rainfall algorithm (GMSRA). *Journal of Applied Meteorology and Climatology*, *40*, 1500–1514. https://doi.org/10.1175/1520-0450(2001)040<1500:GMRAG>2.0.CO;2

Bang, S. D., & Cecil, D. J. (2019). Constructing a multifrequency passive microwave hail retrieval and climatology in the GPM domain. *Journal of Applied Meteorology and Climatology*, *58*, 1889–1904. https://doi.org/10.1175/JAMC-D-19-0042.1

Barnes, H. C., Zuluaga, M. D., & Houze Jr., R. A. (2015). Latent heating characteristics of the MJO computed from TRMM Observations. *Journal of Geophysical Research: Atmospheres*, *120*, 1322–1334. https://doi.org/10.1002/2014JD022530

Battaglia, A., Tanelli, S., Kobayashi, S., Zrnic, D., Hogan, R. J., & Simmer, C. (2010). Multiple-scattering in radar systems: A review. *Journal of Quantitative Spectroscopy & Radiative Transfer*, *111*(6), 917–947. https://doi.org/10.1016/j.jqsrt.2009.11.024

Battaglia, A., Kollias, P., Dhillon, R., Roy, R., Tanelli, S., Lebsock, M., et al. (2020a). Spaceborne cloud and precipitation radars: Status, challenges, and ways forward. *Reviews of Geophysics*, *58*(3), e2019RG000686. https://doi.org/10.1029/2019RG000686

Battaglia, A., Tanelli, S., Tridon, F., Kneifel, S., Leinonen, J., & Kollias, P. (2020b). Triple-frequency radar retrievals. In V. Levizzani, C. Kidd, D. B. Kirschbaum, C. D. Kummerow, K. Nakamura, & F. J. Turk (Eds.), *Satellite precipitation measurement, advances in global change research* (Vol. 67, pp. 211–229). Cham: Springer. https://doi.org/10.1007/978-3-030-24568-9_13

Behrangi, A., Hsu, K., Imam, B., Sorooshian, S., Huffman, G. J., & Kuligowski, R. J. (2009). PERSIANN-MSA: A precipitation estimation method from satellite-based multispectral analysis. *Journal of Hydrometeorology*, *10*(6), 1414–1429. https://doi.org/10.1175/2009JHM1139.1

Bellerby, T. J. (2004). A feature-based approach to satellite precipitation monitoring using geostationary IR imagery. *Journal of Hydrometeorology*, *5*, 910–921. https://doi.org/10.1175/1525-7541(2004)005<0910:AFATSP>2.0.CO;2

Berg, W., LEcuyer, T., & Haynes, J. M. (2010). The distribution of rainfall over oceans from spaceborne radars. *Journal of Applied Meteorology and Climatology*, *49*(3), 535–543. https://doi.org/10.1175/2009JAMC2330.1

Bergeron, T. (1935). On the physics of cloud and precipitation. In *Proceedings of the 5th General Assembly of the UGGI* (Vol. 2, pp. 156–175) UGGI, Lisbon.

Blackwell, W. J., Braun, S., Bennartz, R., Velden, C., DeMaria M., Atlas, R., et al. (2018). An overview of the TROPICS NASA Earth venture mission. *Quarterly Journal of the Royal Meteorological Society*, *144*(S1), 16–26. https://doi.org/10.1002/qj.3290

Bodas-Salcedo, A., Webb, M. J., Bony, S., Chepfer, H., Dufresne, J., Klein, S. A., et al. (2011). COSP: Satellite simulation software for model assessment. *Bulletin of the American Meteorological Society*, *92*(8), 1023–1043. https://doi.org/10.1175/2011BAMS2856.1

Bodas-Salcedo, A., Williams, K. D., Field, P. R., & Lock, A. P. (2012). Downwelling solar radiation surplus over the Southern Ocean in the Met Office Model: The role of midlatitude cyclone clouds. *Journal of Climate*, *25*, 7467–7486. https://doi.org/10.1175/JCLI-D-11-00702.1

Bodas-Salcedo, A., Williams, K. D., Ringer, M. A., Beau, I., Cole, J. N. S., Dufresne, J.-L., et al. (2014). Origins of the solar radiation biases over the Southern Ocean in CFMIP2 models. *Journal of Climate*, *27*(1), 41–56. https://doi.org/10.1175/JCLI-D-13-00169.1

Bodas-Salcedo, A., Hill, P. G., Furtado, K., Williams, K. D., Field, P. R., Manners, J. C., et al. (2016). Large contribution of supercooled liquid clouds to the solar radiation budget of the Southern Ocean. *Journal of Climate*, *29*(11), 4213–4228. https://doi.org/10.1175/JCLI-D-15-0564.1

Boening, C., Lebsock, M., Landerer, F., & Stephens, G. (2012). Snowfall-driven mass change on the East Antarctic ice sheet. *Geophysical Research Letters*, *39*, L21501. https://doi.org/10.1029/2012GL053316

Chang, K.-W., & L'Ecuyer, T. (2019). Role of latent heating vertical distribution in the formation of the tropical cold trap. *Journal of Geophysical Research: Atmospheres*, *124*, 7836–7851. https://doi.org/10.1029/2018JD030194

Cesana, G., & Storelvmo, T. (2017). Improving climate projections by understanding how cloud phase affects radiation. *Journal of Geophysical Research: Atmospheres*, *122*, 4594–4599. https://doi.org/10.1002/2017JD026927

Dai, A. (2006). Precipitation characteristics in eighteen coupled climate models. *Journal of Climate*, *19*(18), 4605–4630. https://doi.org/10.1175/JCLI3884.1

Findeisen, W. (1938). Kolloid-meteorologische Vorgänge bei Niederschlagsbildung. *Meteorologische Zeitschrift*, *55*, 121–133. (trans. and ed. by E. Volken, A.M. Giesche, & S. Brönnimann, (2015). *Meteorologische Zeitschrift*, *24*(4), 443–454. https://doi.org/10.1127/metz/2015/0675).

Fiolleau, T. & Roca, R. (2013). Composite life cycle of tropical mesoscale convective systems from geostationary and low Earth orbit satellite observations: Method and sampling considerations. *Quarterly Journal of the Royal Meteorological Society*, *139*, 941–953. https://doi.org/10.1002/qj.2174

Forbes, R. M., & Ahlgrimm, M. (2014). On the representation of high-latitude boundary layer mixed-phase cloud in the ECMWF global model. *Monthly Weather Review*, *142*(9), 3425–3445. https://doi.org/10.1175/MWR-D-13-00325.1

Forbes, R., Geer, A., Lonitz, K., & Ahlgrimmm M. (2016). Reducing systematic errors in cold-air outbreaks. *ECMWF Newsletter*, *146*, 17–22. https://doi.org/10.21957/s41h7q7l

Gingrey, A., Varble, A., & Zipser, E. (2018). Relationships between extreme rain rates and convective intensities from the perspectives of TRMM and WSR-88D radars. *Journal of Applied Meteorology and Climatology*, *57*(6), 1353–1369. https://doi.org/10.1175/JAMC-D-17-0240.1

Golaz, J.-C., Horowitz, L. W., & Levy II, H. (2013). Cloud tuning in a coupled climate model: Impact on 20th century warming. *Geophysical Research Letters*, *40*, 2246–2251. https://doi.org/10.1002/grl.50232

10.1002/9781119700357.ch15, Downloaded from https://agupubs.onlinelibrary.wiley.com/doi/10.1002/9781119700357.ch15 by Maki Kikuchi - Cochrane Japan , Wiley Online Library on [21/12/2023]. See the Terms and Conditions (https://onlinelibrary.wiley.com/terms-and-conditions) on Wiley Online Library for rules of use; OA articles are governed by the applicable Creative Commons License

Grecu, M., Olson, W. S., Munchak, S. J., Ringerud, S., Liao, L., Haddad, Z. S., et al. (2016). The GPM combined algorithm. *Journal of Atmospheric and Oceanic Technology*, *33*(10), 2225–2245. https://doi.org/10.1175/JTECH-D-16-0019.1

Grody, N. C. (1991). Classification of snow cover and precipitation using the special sensor microwave imager. *Journal of Geophysical Research: Atmospheres*, *96*(D4), 7423–7435. https://doi.org/10.1029/91JD00045

Hagihara, Y., Ohno, Y., Horie, H., Roh, W., Satoh, M., Kubota, T., & Oki, R. (2021). Assessments of Doppler velocity errors of EarthCARE cloud profiling radar using global cloud system resolving simulations: Effects of Doppler broadening and folding. *IEEE Transactions on Geoscience and Remote Sensing, accepted.* https://doi.org/10.1109/TGRS.2021.3060828

Hamada, A., Takayabu, Y. N., Liu, C., & Zipser, E. J. (2015). Weak linkage between the heaviest rainfall and tallest storms. *Nature Communications*, *6*, 6213. https://doi.org/10.1038/ncomms7213

Hashino, T., Satoh, M., Hagihara, Y., Kubota, T., Matsui, T., Nasuno, T., & Okamoto, H. (2013). Evaluating cloud microphysics from NICAM against CloudSat and CALIPSO. *Journal of Geophysical Research: Atmospheres*, *118*, 7273–7292. https://doi.org/10.1002/jgrd.50564

Haynes, J. M., Marchand, R. T., Luo, Z., Bodas-Salcedo, A., & Stephens, G. L. (2007). A multipurpose radar simulation package: QuickBeam. *Bulletin of the American Meteorological Society*, *88*(11), 1723–1727. https://doi.org/10.1175/BAMS-88-11-1723

Hitschfeld, W., & Bordan, J. (1954). Errors inherent in the radar measurement of rainfall at attenuating wavelengths. *Journal of Meteorology*, *11*, 58–67. https://doi.org/10.1175/1520-0469(1954)011<0058:EIITRM>2.0.CO;2

Hollinger, J., Lo, R., & Poe, G. (1987). *Special sensor microwave/imager user's guide*. Washington, DC: Naval Research Laboratory.

Hong, Y., Hsu, K.-L., Sorooshian, S., & Gao, X. (2004). Precipitation estimation from remotely sensed imagery using an acritical neural network cloud classification system. *Journal of Applied Meteorology and Climatology*, *43*, 1834–1853. https://doi.org/10.1175/JAM2173.1

Hogan, R., & Battaglia, A. (2008). Fast lidar and radar multiple-scattering models. Part 2: Wide-angle scattering using the time-dependent two-stream approximation. *Journal of the Atmospheric Sciences*, *65*(12), 3636–3651. https://doi.org/10.1175/2008JAS2643.1

Hou, A. Y., Kakar, R. K., Neeck, S., Azarbarzin, A. A., Kummerow, C. D., Kojima, M., et al. (2014). The global precipitation measurement mission. *Bulletin of the American Meteorological Society*, *95*, 701–722. https://doi.org/10.1175/BAMS-D-13-00164.1

Houze Jr., R. A., Rasmussen, K. L., Zuluaga, M. D., & Brodzik, S. R. (2015). The variable nature of convection in the tropics and subtropics: A legacy of 16 years of the Tropical Rainfall Measuring Mission satellite. *Reviews of Geophysics*, *53*(3), 994–1021. https://doi.org/10.1002/2015RG000488

Huffman, G. J., Bolvin, D. T., Nelkin, E. J., Wolff, D. B., Adler, R. E., Gu, G., et al. (2007). The TRMM multi-satellite precipitation analysis: Quasi-global, multi-year, combined-sensor precipitation estimates at fine scale. *Journal of Hydrometeorology*, *8*, 38–55. https://doi.org/10.1175/JHM560.1

Hsu, K.-L., & Sorooshian, S. (2009). Satellite-based precipitation measurement using PERSIANN system. In S. Sorooshian, K.-L. Hsu, E. Coppola, B. tomasserti, M. Verdecchia & G. Visconti (Eds.), *Hydrological modeling and the water cycle* (pp. 27–48). Berlin/Heidelberg: Springer. ISBN: 978-3-540-77843-1.

Huaman, L., & Schumacher, C. (2018). Assessing the vertical latent heating structure of the east Pacific ITCZ using the CloudSat CPR and TRMM PR. *Journal of Climate*, *31*, 2563–2577. https://doi.org/10.1175/JCLI-D-17-0590.1

Huang, Y., Siems, S. T., Manton, M. J., Protat, A., & Delanoë, J. (2012). A study on the low-altitude clouds over the Southern Ocean using the DARDAR-MASK. *Journal of Geophysical Research: Atmospheres*, *117*, D18204. https://doi.org/10.1029/2012JD017800

Iguchi, T. (2020). Dual-frequency Precipitation Radar (DPR) on the Global Precipitation Measurement (GPM) mission's core observatory. In V. Levizzani, C. Kidd, D. B. Kirschbaum, C. D. Kummerow, K. Nakamura, & F. J. Turk (Eds.), *Satellite precipitation measurement, advances in global change research* (Vol. 67, pp. 183–192). Cham: Springer. https://doi.org/10.1007/978-3-030-24568-9_11

Iguchi, T., & Haddad, Z., (2020). Introduction to radar rain retrieval methods. In V. Levizzani, C. Kidd, D. B. Kirschbaum, C. D. Kummerow, K. Nakamura, & F. J. Turk (Eds.), *Satellite precipitation measurement, advances in global change research* (Vol. 67, pp 169–182). Cham: Springer. https://doi.org/10.1007/978-3-030-24568-9_10

Illingworth, A. J., Barker, H. W., Beljaars, A., Ceccaldi, M., Chepfer, H., Clerbaux, N., et al. (2015). The EarthCARE satellite: The next step forward in global measurements of clouds, aerosols, precipitation, and radiation. *The Bulletin of the American Meteorological Society*, *96*. https://doi.org/10.1175/BAMS-D-12-00227.1

Jing, X., & Suzuki, K., (2018). The impact of process-based warm rain constraints on the aerosol indirect effect. *Geophysical Research Letters*, *45*, 10729–10737. https://doi.org/10.1029/2018GL079956

Jing, X., Suzuki, K., Guo, H., Goto, D., Ogura, T., Koshiro, T., & Mulmenstadt, J. (2017). A multi-model study on warm precipitation biases in global models compared to satellite observations. *Journal of Geophysical Research: Atmospheres*, *122*, 11806–11824. https://doi.org/10.1002/2017JD027310

Jing, X., Suzuki, K., & Michibata, T. (2019). The key role of warm rain parameterization in determining the aerosol indirect effect in a global climate model. *Journal of Climate*, *32*, 4409–4430. https://doi.org/10.1175/JCLI-D-18-0789.1

Joyce, R. J., & Xie, P. (2011). Kalman filter-based CMORPH. *Journal of Hydrometeorology*, *12*, 1547–1563. https://doi.org/10.1175/JHM-D-11-022.1

Kawai, H., Yukimoto, S., Koshiro, T., Oshima, N., Tanaka, T., Yoshimura, H., & Nagasawa, R. (2019). Significant improvement of cloud representation in the global climate model MRI-ESM2. *Geoscientific Model Development*, *12*, 2875–2897. https://doi.org/10.5194/gmd-12-2875-2019

Kay, J. E., Bourdages, L., Miller, N. B., Morrison, A., Yettella, V., Chepfer, H., & Eaton, B. (2016). Evaluating and improving

10.1002/9781119700357.ch15, Downloaded from https://agupubs.onlinelibrary.wiley.com/doi/10.1002/9781119700357.ch15 by Maki Kikuchi - Cochrane Japan , Wiley Online Library on [21/12/2023]. See the Terms and Conditions (https://onlinelibrary.wiley.com/terms-and-conditions) on Wiley Online Library for rules of use; OA articles are governed by the applicable Creative Commons License

cloud phase in the Community Atmosphere Model version 5 using spaceborne lidar observations. *Journal of Geophysical Research: Atmospheres*, *121*, 4162– 4176. https://doi.org/10.1002/2015JD024699

Kay, J. E., L'Ecuyer, T., Pendergrass, A., Chepfer, H., Guzman, R., & Yettella, V. (2018). Scale-aware and definition-aware evaluation of modeled near-surface precipitation frequency using CloudSat observations. *Journal of Geophysical Research: Atmospheres*, *123*, 4294–4309. https://doi.org/10.1002/2017JD028213

Kidd, C., Becker, A., Huffman, G. J., Muller, C.L., Joe, P., Skofronick-Jackson, G., & Kirschbaum, D. B. (2017). So, how much of the Earth's surface is covered by rain gauges? *Bulletin of the American Meteorological Society*, *98*, 69–78. https://doi.org/10.1175/BAMS-D-14-00283.1

Kidd, C., Takayabu, Y. N., Skofronick-Jackson, G. M., Huffman, G. J., Braun, S. A., Kubota, T., & Turk, F. J. (2020). The Global Precipitation Measurement (GPM) mission. In V. Levizzani, C. Kidd, D. B. Kirschbaum, C. D. Kummerow, K. Nakamura, & F. J. Turk (Eds.), *Satellite precipitation measurement, advances in global change research* (Vol. 67, pp. 3–23). Cham: Springer Nature. https://doi.org/10.1007/978-3-030-24568-9_1

Kikuchi, M., & Suzuki, K. (2019). Characterizing vertical particle structure of precipitating cloud system from multiplatform measurements of A-Train constellation. *Geophysical Research Letters*, *46*, 1040–1048. https://doi.org/10.1029/2018GL081244

Kilic, L., Prigent, C., Boutin, J., Meissner, T., English, S., & Yueh, S. (2019). Comparisons of ocean radiative transfer models with SMAP and AMSR2 observations. *Journal of Geophysical Research: Oceans*, *124*, 7683–7699. https://doi.org/10.1029/2019JC015493

Kollias, P., Tanelli, S., Battaglia, A., & Tatarevic, A. (2014). Evaluation of EarthCARE cloud profiling radar Doppler velocity measurements in particle sedimentation regimes. *Journal of Atmospheric and Oceanic Technology*, *31*(2), 366–386. https://doi.org/10.1175/JTECH-D-11-00202.1

Kubar, T. L., Hartmann, D. L., & Wood, R. (2009). Understanding the importance of microphysics and macrophysics for warm rain in marine low clouds. Part I: Satellite observations. *Journal of the Atmospheric Sciences*, *66*, 2953–2972. https://doi.org/10.1175/2009JAS3071.1

Kummerow, C. D. (2020). Introduction to passive microwave retrieval methods. In V. Levizzani, C. Kidd, D. B. Kirschbaum, C. D. Kummerow, K. Nakamura, & F. J. Turk (Eds.), *Satellite precipitation measurement, advances in global change research* (Vol. 67, pp. 123–140). Cham: Springer Nature. https://doi.org/10.1007/978-3-030-24568-9_7.

Kummerow, C. D., Randel, D. L., Kulie, M., Wang, N., Ferraro, R., Munchak, S. J., & Petkovic, V. (2015). The evolution of the Goddard profiling algorithm to a fully parametric scheme. *Journal of Atmospheric and Oceanic Technology*, *32*, 2265–2280. https://doi.org/:10.1175/jtech-d-15-0039.1.

Kummerow, C., Simpson, J., Thiele, O., Barnes, W., Chang, A. T. C., Stocker, E., et al. (2000). The status of the Tropical Rainfall Measuring Mission (TRMM) after two years in orbit. *Journal of Applied Meteorology and Climatology*, *39*, 1965–1982. https://doi.org/10.1175/1520-0450(2001)040%3C1965:TSOTTR%3E2.0.CO;2

Kuo, Y., Neelin, J. D., Chen, C., Chen, W., Donner, L. J., Gettelman, A., et al. (2020). Convective transition statistics over tropical oceans for climate model diagnostics: GCM evaluation. *Journal of the Atmospheric Sciences*, *77*(1), 379–403. https://doi.org/10.1175/JAS-D-19-0132.1

Lebsock, M., Stephens, G. L., & Kummerow, C. (2008). Multisensor satellite observations of aerosol effects on warm clouds. *Journal of Geophysical Research: Atmospheres*, *113*, D15205. https://doi.org/10.1029/2008JD009876

Lebsock, M. D., L'Ecuyer, T. S., Wood, N. B., Haynes, J. M. & Smalley, M. A. (2020). Status of the CloudSat mission. In V. Levizzani, C. Kidd, D. B. Kirschbaum, C. D. Kummerow, K. Nakamura, & F. J. Turk (Eds.), *Satellite precipitation measurement, advances in global change research* (Vol. 67, pp. 211–229). Cham: Springer Nature. https://doi.org/10.1007/978-3-030-24568-9_2

Leon, D. C., Wang, Z., & Liu, D. (2008). Climatology of drizzle in marine boundary layer clouds based on 1 year of data from CloudSat and Cloud-Aerosol Lidar and Infrared Pathfinder Satellite Observations (CALIPSO). *Journal of Geophysical Research: Atmospheres*, *113*, D00A14. https://doi.org/10.1029/2008JD009835

L'Ecuyer, T. S., & Stephens, G. L. (2002). An estimation-based precipitation retrieval algorithm for attenuating radars. *Journal of Applied Meteorology and Climatology*, *41*(3), 272–285. https://doi.org/10.1175/1520-0450(2002)041%3C0272:AEBPRA%3E2.0.CO;2

L'Ecuyer, T. S., Berg, W., Haynes, J., Lebsock, M., & Takemura, T. (2009). Global observations of aerosol impacts on precipitation occurrence in warm maritime clouds. *Journal of Geophysical Research: Atmospheres*, *114*, D09211. https://doi.org/10.1029/2008JD011273

Letu, H., Nagao, T. M., Nakajima, T. Y., Riedi, J., Ishimoto, H., Baran, A. J., et al. (2019). Ice cloud properties from Himawari-8/AHI next-generation geostationary satellite: Capability of the AHI to monitor the DC cloud generation process. *IEEE Transactions on Geoscience and Remote Sensing*, *57*. https://doi.org/10.1109/TGRS.2018.2882803

Lhermitte, R. (1990). Attenuation and scattering of millimeter wavelength radiation by clouds and precipitation. *Journal of Atmospheric and Oceanic Technology*, *7*, 464–479. https://doi.org/10.1175/1520-0426(1990)007%3C0464:AASOMW%3E2.0.CO;2

Liu, G. (2008). A database of microwave single-scattering properties for nonspherical ice particles. *Bulletin of the American Meteorological Society*, *89*, 1563–1570. https://doi.org/10.1175/2008bams2486.1

Liu, C., Shige, S., Takayabu, Y., & Zipser, E. (2015). Latent heating contribution from precipitation systems with different sizes, depths, and intensities in the tropics. *Journal of Climate*, *28*, 186–203. https://doi.org/10.1175/JCLI-D-14-00370.1

Luo, Z. J., Liu, G. Y., Stephens, G. L., & Johnson, R. H. (2009). Terminal versus transient cumulus congestus: A CloudSat perspective. *Geophysical Research Letters*, *36*, L05808. https://doi.org/10.1029/2008GL036927

Luo, Z. J., Liu, G. Y., & Stephens, G. L. (2010). Use of A-Train data to estimate convective buoyancy and entrainment rate.

10.1002/9781119700357.ch15, Downloaded from https://agupubs.onlinelibrary.wiley.com/doi/10.1002/9781119700357.ch15 by Maki Kikuchi - Cochrane Japan , Wiley Online Library on [21/12/2023]. See the Terms and Conditions (https://onlinelibrary.wiley.com/terms-and-conditions) on Wiley Online Library for rules of use; OA articles are governed by the applicable Creative Commons License

Geophysical Research Letters, *37*, L09804. https://doi.org/10.1029/2010GL042904

Luo, Z. J., Jeyaratnam, J., Iwasaki, S., Takahashi, H., & Anderson, R. (2014). Convective vertical velocity and cloud internal vertical structure: An A-Train perspective. *Geophysical Research Letters*, *41*. https://doi.org/10.1002/2013GL058922

Luo, Z. J., Anderson, R., Rossow, W. B., & Takahashi, H. (2017). Tropical cloud and precipitation regimes as seen from near-simultaneous TRMM, CloudSat, and CALIPSO observations and comparison with ISCCP. *Journal of Geophysical Research: Atmospheres, 122*. https://doi.org/10.1002/2017JD026569

Marra, A. C., Porcu, F., Baldini, L., Petracca, M., Casella, D., Dietrich, S., et al. (2017). Observational analysis of an exceptionally intense hailstorm over the Mediterranean area: Role of the GPM core observatory. *Atmospheric Research*, *192*, 72–90. https://doi.org/10.1016/j.atmosres.2017.03.019

Masunaga, H., Matsui, T., Tao, W., Hou, A. Y., Kummerow, C. D., Nakajima, T., et al. (2010). Satellite data simulator unit: A multisensor, multispectral satellite simulator package. *Bulletin of the American Meteorological Society*, *91*, 1625–1632. https://doi.org/10.1175/2010BAMS2809.1

Masunaga, H. (2012). A satellite study of the atmospheric forcing and response to moist convection over tropical and subtropical oceans. *Journal of the Atmospheric Sciences*, 150–167. https://doi.org/10.1175/JAS-D-11-016.1

Masunaga, H. (2013). A satellite study of tropical moist convection and environmental variability: A moisture and thermal budget analysis. *Journal of the Atmospheric Sciences*, *70*, 2443–2465. https://doi.org/10.1175/JAS-D-12-0273.1

Masunaga, H., & Bony, S. (2018). Radiative invigoration of tropical convection by preceding cirrus clouds. *Journal of the Atmospheric Sciences*, *75*, 1327–1342. https://doi.org/10.1175/JAS-D-17-0355.1

Masunaga, H., & Luo, Z. J. (2016). Convective and large-scale mass flux profiles over tropical oceans determined from synergistic analysis of a suite of satellite observations. *Journal of Geophysical Research: Atmospheres*, *121*, 7958–7974. https://doi.org/10.1002/2016JD024753

Mathew, S. S., & Kumar, K. K. (2019). On the role of precipitation latent heating in modulating the strength and width of the Hadley circulation. *Theoretical and Applied Climatology*, *136*, 661–673. https://doi.org/10.1007/s00704-018-2515-4

McIlhattan, E. A., L'Ecuyer, T. S., & Miller, N. B. (2017). Observational evidence linking Arctic supercooled liquid cloud biases in CESM to snowfall processes. *Journal of Climate*, *30*(12), 4477–4495. https://doi.org/10.1175/JCLI-D-16-0666.1

Meneghini, R., Kim, H., Liao, L., Jones, J. A., & Kwiatkowski, J. M. (2015). An initial assessment of the surface reference technique applied to data from the Dual-Frequency Precipitation Radar (DPR) on the GPM satellite. *Journal of Atmospheric and Oceanic Technology*, *32*, 2281–2296. https://doi.org/10.1175/JTECH-D-15-0044.1

Michibata, T., Suzuki, K., Sekiguchi, M., & Takemura, T. (2019). Prognostic precipitation in the MIROC6-SPRINTARS GCM: Description and evaluation against satellite observations. *Journal of Advances in Modeling Earth Systems*, *11*, 839–860. https://doi.org/10.1029/2018MS001596

Michibata, T., & Suzuki, K. (2020). Reconciling compensating errors between precipitation constraints and the energy budget in a climate model. *Geophysical Research Letters*, *47*, e2020GL088340. https://doi.org/10.1029/2020GL088340

Morrison, H., de Boer, G., Feingold, G., Harrington, J., Shupe, M. D., & Sulia, K. (2012). Resilience of persistent Arctic mixed-phase clouds. *Nature Geoscience*, *5*, 11–17. https://doi.org/10.1038/ngeo1332

Mroz, K., Battaglia, A., Lang, T. J., Tanelli, S., & Sacco, G. F. (2018). Global precipitation measuring Dual-Frequency Precipitation Radar observations of hailstorm vertical structure: Current capabilities and drawbacks. *Journal of Applied Meteorology and Climatology*, *57*, 2161–2178. https://doi.org/10.1175/JAMC-D-18-0020.1

Nakamura, K. (1991). Biases of rain retrieval algorithms for spaceborne radar caused by nonuniformity of rain. *Journal of Atmospheric and Oceanic Technology*, *8*, 363–373. https://doi.org/10.1175/1520-0426(1991)008<0363:BORRAF>2.0.CO;2

Nakajima, T. Y., Suzuki, K., & Stephens, G. L. (2010). Droplet growth in warm water clouds observed by the A-Train. Part II: A multisensor view. *Journal of the Atmospheric Sciences*, *67*, 1897–1907. https://doi.org/10.1175/2010JAS3276.1

National Academies of Sciences, Engineering, and Medicine (2018). *Thriving on our changing planet: A decadal strategy for Earth observation from space*. Washington, DC: The National Academies Press. https://doi.org/10.17226/24938

Nowell, H., Liu, G., & Honeyager, R. (2013). Modeling the microwave single-scattering properties of aggregate snowflakes. *Journal of Geophysical Research: Atmospheres*, *118*, 7873–7885. https://doi.org/10.1002/jgrd.50620

Okamoto K. (2003). A short history of the TRMM precipitation radar. In W. K. Tao, & R. Adler (Eds.), *Cloud systems, hurricanes, and the Tropical Rainfall Measuring Mission (TRMM), meteorological monographs*. Boston, MA: American Meteorological Society. https://doi.org/10.1007/978-1-878220-63-9_16

Palerme, C., Genthon, C., Claud, C., Kay, J. E., Wood, N. B., & L'Ecuyer, T. (2017). Evaluation of current and projected Antarctic precipitation in CMIP5 models. *Climate Dynamics*, *48*, 225–239. https://doi.org/10.1007/s00382-016-3071-1

Protat, A., Klepp, C., Louf, V., Petersen, W. A., Alexander, S. P., Barros, A., et al. (2019). The latitudinal variability of oceanic rainfall properties and its implication for satellite retrievals: 1. Drop size distribution properties. *Journal of Geophysical Research: Atmospheres*, *124*(23), 13291–13311. https://doi.org/10.1029/2019JD031010

Reitter, S., Fröhlich, K., Seifert, A., Crewell, S., & Mech, M. (2011). Evaluation of ice and snow content in the global numerical weather prediction model GME with CloudSat. *Geoscientific Model Development*, *4*(3), 579–589. https://doi.org/10.5194/gmd-4-579-2011

Sauter, K., & L'Ecuyer, T. S. (2017). Observational evidence for the vertical redistribution and scavenging of Saharan dust by tropical cyclones. *Geophysical Research Letters*, *44*, 6421–6430. https://doi.org/10.1002/2017GL074166

10.1002/9781119700357.ch15, Downloaded from https://agupubs.onlinelibrary.wiley.com/doi/10.1002/9781119700357.ch15 by Maki Kikuchi - Cochrane Japan , Wiley Online Library on [21/12/2023]. See the Terms and Conditions (https://onlinelibrary.wiley.com/terms-and-conditions) on Wiley Online Library for rules of use; OA articles are governed by the applicable Creative Commons License

Sauter, K., L'Ecuyer, T. S., van den Heever, S. C., Twohy, C., Heidinger, A., Wanzong, S., & Wood, N. (2019). The observed influence of tropical convection on the Saharan dust layer. *Journal of Geophysical Research: Atmospheres*, *124*, 10896–10912. https://doi.org/10.1029/2019JD031365

Schumacher, C., Houze, R. A., & Kraucunas, I. (2004). The tropical dynamical response to latent heating estimates derived from the TRMM precipitation radar. *Journal of the Atmospheric Sciences*, *61*, 1341–1358. https://doi.org/10.1175/1520-0469(2004)061<1341:TTDRTL>2.0.CO;2

Seto, S., & Iguchi, T. (2015). Intercomparison of attenuation correction methods for the GPM Dual-Frequency Precipitation Radar. *Journal of Atmospheric and Oceanic Technology*, *32*, 915–926. https://doi.org/10.1175/JTECH-D-14-00065.1

Seto, S., Iguchi, T., Shimozuma, T., & Hayashi, S. (2015). NUBF correction methods for the GPM/DPR level-2 algorithms. *IEEE International Geoscience Remote Sensing Symposium (IGARSS)*, 2612–2614. https://doi.org/10.1109/IGARSS.2015.7326347

Shupe, M. D. (2011). Clouds at Arctic atmospheric observatories. Part II: Thermodynamic phase characteristics. *Journal of Applied Meteorology and Climatology*, *50*(3), 645–661. https://doi.org/10.1175/2010JAMC2468.1

Simpson, J., Adler, R. F., & North, G. R. (1988). A proposed Tropical Rainfall Measuring Mission (TRMM) satellite. *Bulletin of the American Meteorological Society*, *69*, 278–295. https://doi.org/10.1175/1520-0477(1988)069<0278:APTRMM>2.0.CO;2

Skofronick-Jackson, G., Kirschbaum, D., Petersen, W., Huffman, G., Kidd, C., Stocker, E., & Kakar, R. (2018). The Global Precipitation Measurement (GPM) mission's scientific achievements and societal contributions: Reviewing four years of advanced rain and snow observations. *Quarterly Journal of the Royal Meteorological Society*, *144*(S1), 27–48. https://doi.org/2789 10.1002/qj.3313

Sohn, B. J., Ryu, G., Song, H., & Ou, M. (2013). Characteristic features of warm-type rain producing heavy rainfall over the Korean Peninsula inferred from TRMM measurements. *Monthly Weather Review*, *141*(11), 3873–3888. https://doi.org/10.1175/MWR-D-13-00075.1

Sorooshian, A., Feingold, G., Lebsock, M. D., Jiang, H., & Stephens, G. L. (2009). On the precipitation susceptibility of clouds to aerosol perturbations. *Geophysical Research Letters*, *36*, L13803. https://doi.org/10.1029/2009GL038993

Stephens, G. L., L'Ecuyer, T., Forbes, R., Gettelman, A., Golaz, J.-C., Bodas-Salcedo, A., et al. (2010). Dreary state of precipitation in global models. *Journal of Geophysical Research: Atmospheres*, *115*, D24211. https://doi.org/10.1029/2010JD014532

Stephens, G., Winker, D., Pelon, J., Trepte, C., Vane, D., Yuhas, C., et al. (2018). CloudSat and CALIPSO within the A-Train: Ten years of actively observing the Earth system. *Bulletin of the American Meteorological Society*, *99*, 569–581. https://doi.org/10.1175/BAMS-D-16-0324.1

Stephens, G. L., Smalley, M. A., & Lebsock, M. D. (2019a). The cloudy nature of tropical rains. *Journal of Geophysical Research: Atmospheres*, *124*, 171–188. https://doi.org/10.1029/2018JD029394

Stephens, G. L., Christensen, M., Andrews, T., Haywood, J., Malavelle, F. F., Suzuki, K., et al. (2019b). Cloud physics from space. *Quarterly Journal of the Royal Meteorological Society*, *145*, 2854–2875. https://doi.org/10.1002/qj.3589

Storelvmo, T., Tan, I., & Korolev, A.V. (2015). Cloud phase changes induced by CO2 warming—a powerful yet poorly constrained cloud-climate feedback. *Current Climate Change Reports*, *1*, 288–296. https://doi.org/10.1007/s40641-015-0026-2

Suzuki, K., Nakajima, T. Y., & Stephens, G. L. (2010). Particle growth and drop collection efficiency of warm clouds as inferred from joint CloudSat and MODIS observations. *Journal of Geophysical Research: Atmospheres*, *67*, 3019–3032. https://doi.org/10.1175/2010JAS3463.1

Suzuki, K., Stephens, G. L., van den Heever, S. C., & Nakajima, T. Y. (2011). Diagnosis of the warm rain process in cloud-resolving models using joint CloudSat and MODIS observations. *Journal of the Atmospheric Sciences*, *68*, 2655–2670. https://doi.org/10.1175/JAS-D-10-05026.1

Suzuki, K., Golaz, J.-C., & Stephens, G. L. (2013). Evaluating cloud tuning in a climate model with satellite observations. *Geophysical Research Letters*, *40*, 4464–4468. https://doi.org/10.1002/grl.50874

Suzuki, K., Stephens, G., Bodas-Salcedo, A., Wang, M., Golaz, J.-C., Yokohata, T., & Koshiro, T. (2015). Evaluation of the warm rain formation process in global models with satellite observations. *Journal of the Atmospheric Sciences*, *72*, 3996–4014. https://doi.org/10.1175/JAS-D-14-0265.1

Takahashi, H., & Luo, Z. J. (2014). Characterizing tropical overshooting deep convection from joint analysis of CloudSat and geostationary satellite observations. *Journal of Geophysical Research: Atmospheres*, *119*, 112–121. https://doi.org/10.1002/2013JD020972

Tan, I., Storelvmo, T., & Zelinka, M. D. (2016). Observational constraints on mixed-phase clouds imply higher climate sensitivity. *Science*, *352*(6282), 224–227. https://doi.org/10.1126/science.aad5300

Tan, I., & Storelvmo, T. (2019). Evidence of strong contributions from mixed-phase clouds to Arctic climate change. *Geophysical Research Letters*, *46*, 2894–2902. https://doi.org/10.1029/2018GL081871

Tanelli, S., Durden, S. L., Im, E., Pak, K. S., Reinke, D. G., Partain, P., et al. (2008). CloudSat's cloud profiling radar after two years in orbit: Performance, calibration, and processing. *IEEE Transactions on Geoscience and Remote Sensing*, *46*(11), 3560–3573. https://doi.org/10.1109/TGRS.2008.2002030

Trenberth, K. E., & Fasullo, J. T. (2010). Simulation of present-day and twenty-first-century energy budgets of the Southern Oceans. *Journal of Climate*, *23*, 440–454. https://doi.org/10.1175/2009JCLI3152.1

Ushio, T., Kubota, T., Shige, S., Okamoto, K., Aonashi, K., Inoue, T., et al. (2009). A Kalman filter approach to the Global Satellite Mapping of Precipitation (GSMaP) from combined passive microwave and infrared radiometric data. *Journal of the Meteorological Society of Japan*, *87A*, 137–151. https://doi.org/10.2151/jmsj.87A.137

Vincent, C. L., & Lane, T. P. (2018). Mesoscale variation in diabatic heating around Sumatra, and its modulation with the

10.1002/9781119700357.ch15, Downloaded from https://agupubs.onlinelibrary.wiley.com/doi/10.1002/9781119700357.ch15 by Maki Kikuchi - Cochrane Japan , Wiley Online Library on [21/12/2023]. See the Terms and Conditions (https://onlinelibrary.wiley.com/terms-and-conditions) on Wiley Online Library for rules of use; OA articles are governed by the applicable Creative Commons License

Madden–Julian Oscillation. *Monthly Weather Review*, *146*, 2599–2614. https://doi.org/10.1175/MWR-D-17-0392.1

Voors, R., Donovan, D., Acarreta, J., Eisinger, M., Franco, R., Lajas, D., et al. (2007). ECSIM: The simulator framework for EarthCARE. *Proceedings SPIE 6744, Sensors, Systems, and Next-Generation Satellites XI*, 67441Y. https://doi.org/10.1117/12.737738

Wardah, T., Abu Bakar, S. H., Bardossy, A., & Maznorizan, M. (2008). Use of geostationary meteorological satellite images in convective rain estimation for flash-flood forecasting. *Journal of Hydrology*, *356*, 3–4, 283–298. https://doi.org/10.1016/j.jhydrol.2008.04.015

Wang, T., & Tang, G. (2020). Spatial variability and linkage between extreme convections and extreme precipitation revealed by 22-year space-borne precipitation radar data. *Geophysical Research Letters*, *46*, e2020GL088437. https://doi.org/10.1029/2020GL088437

Wang, M., Ghan, S., Liu, X., L'Ecuyer, T. S., Zhang, K., Morrison, H., et al. (2012). Constraining cloud lifetime effects of aerosols using A-Train satellite observations. *Geophysical Research Letters*, *39*, L15709. https://doi.org/10.1029/2012GL052204

Wegener, A. (1911). *Thermodynamik der Atmosphäre* (p. 331). – Leipzig, Germany: Barth.

Wilheit, T. T. (1972). The Electrically Scanning Microwave Radiometer (ESMR) experiment. In R. R. Sabatini (Eds.), *The Nimbus 5 user's guide* (pp. 87–108). Greenbelt, MD: NASA/Goddard Space Flight Center.

Wood, N., &. L'Ecuyer, T. S. (2013). Level 2C snow profile process description and interface control document, version 0. *CloudSat Project: A NASA Earth System Science Pathfinder Mission*, 23. http://www.cloudsat.cira.colostate.edu/sites/

Wood, R., Kubar, T. L., & Hartmann, D. L. (2009). Understanding the importance of microphysics and macrophysics for warm rain in marine low clouds. Part II: Heuristic models of rain formation. *Journal of the Atmospheric Sciences*, *66*, 2973–2990. https://doi.org/10.1175/2009JAS3072.1

10.1002/9781119700357.ch15, Downloaded from https://agupubs.onlinelibrary.wiley.com/doi/10.1002/9781119700357.ch15 by Maki Kikuchi - Cochrane Japan , Wiley Online Library on [21/12/2023]. See the Terms and Conditions (https://onlinelibrary.wiley.com/terms-and-conditions) on Wiley Online Library for rules of use; OA articles are governed by the applicable Creative Commons License